Clim Dyn (2014) 43:3025–3046
DOI 10.1007/s00382-014-2107-7

Seasonal variability of the equatorial undercurrent termination and associated salinity maximum in the Gulf of Guinea

Nicolas Kolodziejczyk · Frédéric Marin · Bernard Bourlès · Yves Gouriou · Henrick Berger

Received: 15 May 2013 / Accepted: 28 February 2014 / Published online: 28 March 2014

Abstract The termination of the Equatorial Undercurrent (EUC) in the eastern equatorial Atlantic during boreal summer and fall, and the fate of the associated saline water masses, are analyzed from in situ hydrological and currents data collected during 19 hydrographic cruises between 2000 and 2007, complemented by observations from Argo profiling floats and PIRATA moorings, and from a numerical simulation of the Tropical Atlantic Ocean for the period 1993–2007. An intense variability of the circulation and hydrological properties is evidenced from observations in the upper thermocline (24.5–26.2 isopycnal layer) between June and November. During early boreal summer, saline water masses are transported eastward in the upper thermocline to the African coast within the EUC, and recirculate westward on both sides of the EUC. In mid-boreal summer, the EUC weakens in the upper thermocline and the equatorial salinity maximum disappears due to intense mixing with the surface waters during the upwelling season. The extra-equatorial salinity maxima are also partially eroded during the boreal summer, with a slight poleward migration of the southern hemisphere maximum until late boreal summer. The upper EUC reappears in September, feeding again the eastern equatorial Atlantic with saline waters until boreal spring. During December–January, numerical results suggest a second seasonal weakening of the EUC in the Gulf of Guinea, with a partial erosion of the associated equatorial salinity maximum.

This paper is a contribution to the special issue on tropical Atlantic variability and coupled model climate biases that have been the focus of the recently completed Tropical Atlantic Climate Experiment (TACE), an international CLIVAR program (http://www.clivar.org/organization/atlantic/tace). This special issue is coordinated by William Johns, Peter Brandt, and Ping Chang, representatives of the TACE Observations and TACE Modeling and Synthesis working groups.

N. Kolodziejczyk (✉)
Sorbonne Universités (UPMC, Univ Paris 06)-CNRS-IRD-MNHN, LOCEAN Laboratory, 4, place Jussieu, 75252 Paris, France
e-mail: nicolas.kolodziejczyk@gmail.com

F. Marin · B. Bourlès
Université de Toulouse, UPS (OMP-PCA), Toulouse, France

F. Marin
IRD, LEGOS, Nouméa, New Caledonia

B. Bourlès
IRD, LEGOS, Plouzané, France

Y. Gouriou
IRD-US191, Plouzané, France

H. Berger
IFREMER, DYNECO-PYSED, Plouzané, France

1 Introduction

The Equatorial UnderCurrent (EUC) is the strongest zonal flow in the tropical Atlantic Ocean, flowing eastward along the equator within the thermocline. It is first the equatorial branch of a large-scale meridional circulation—the Sub-Tropical Cells (STCs)—that consists in the subduction of saline and oxygen-enriched waters in the subtropics, and their advection mainly within the southern thermocline to the equatorial region, via western boundary currents and interior ventilation (e.g., Blanke et al. 2002; Snowden and Molinari 2003; Zhang et al. 2003; Hazeleger et al. 2003). The EUC also contributes to the Atlantic Meridional Overturning circulation (e.g., Lumpkin and Speer 2003; Hazeleger and de Vries 2003; Hazeleger et al. 2003; Chang et al. 2008). Most of EUC water masses then surface in the

central and eastern equatorial Atlantic (Hazeleger and de Vries 2003; Rhein et al. 2010; Jouanno et al. 2011a, b; Hummels et al. 2013).

The pathways of the poleward return surface flow to the mid-latitudes is still very unclear, and float observations (Grodsky and Carton 2002) as well as eddy-resolving models (e.g., Hazeleger and de Vries 2003) indicate multiple recirculations and downwellings of the upwelled waters within the inner tropics (5°S–5°N), forming the so-called Tropical Cells (TCs) (Molinari et al. 2003; Wang 2005). Part of the EUC water masses might also exit directly the equatorial basin through the southward Gabon-Congo Undercurrent (GCUC) along the African coast (Hisard and Morlière 1973; Wacongne and Piton 1992).

Recent observational studies have described the mean properties of the EUC in the Atlantic between the western boundary and 0°E (Schott et al. 1998; Bourlès et al. 1999, 2002; Stramma and Schott 1999; Brandt et al. 2006; Kolodziejczyk et al. 2009; Johns et al. 2014). The core of the EUC is characterized by maximum salinity and dissolved oxygen concentrations, while the mean EUC transport is seen to progressively weaken eastward from 20.9 Sv at 35°W to 9.1 Sv at 0°W (Schott et al. 1998; Johns et al. 2014). East of 0°E, in spite of sparse recent measurements (Hummels et al. 2013), the fate of the EUC remains still poorly documented.

Both numerical and observational studies indicate that the EUC is subject to a strong seasonal cycle (Arhan et al. 2006). At 10°W, Kolodziejczyk et al. (2009) observed two maxima of the EUC transport from individual cruises: the strongest (up to 30.0 Sv) during boreal summer and early fall, and the weakest (up to 14.8 Sv) during boreal winter, but the full seasonal cycle of the EUC transport at that longitude could not be resolved due to the absence of observations during the boreal spring. More recently, Johns et al. (2014) confirmed this semi-annual cycle of the EUC transport at 10°W from current-meter moorings, but the boreal summer maximum was found to be weaker ($\sim$18 Sv) than in Kolodziejczyk et al. (2009), and the second maximum ($\sim$14 Sv) was observed in boreal spring. In the central and eastern equatorial Atlantic, the thermocline and EUC seasonal variability is mainly associated with the basin scale adjustment to the zonal wind forcing over the equatorial Atlantic (e.g., Katz et al. 1981; Philander and Pacanowski 1986; Wacongne 1989; Giarolla et al. 2005; Kolodziejczyk et al. 2009; Johns et al. 2014). East of 0°E, due to sparser observations, the seasonal variability of the EUC termination remains an open question.

Moreover, previous observations have shown a strong seasonal variability of salinity in the thermocline in the eastern equatorial Atlantic. From hydrological measurements collected during 1982–1984, Gouriou and Reverdin (1992) identified the presence of a tongue of high salinity waters during boreal spring over the whole width of the Atlantic Ocean. This tongue reached the eastern boundary, and spread meridionally from 5°S to 5°N (Gouriou and Reverdin 1992; their Fig. 8). Mercier et al. (2003) also observed extra-equatorial salinity maxima around 3°S–N within the upper thermocline during boreal spring 1995 at 3°E, associated with westward circulations surrounding the EUC. During boreal summer, this equatorial salinity maximum is found to weaken or even disappear (Hisard and Morlière 1973; Verstraete 1992; Gouriou and Reverdin 1992).

The EUC additionally exhibits a year-to-year variability over the whole equatorial Atlantic, as evidenced from observations carried out during boreal summer of different years (Gouriou and Reverdin 1992; Bourlès et al. 2002). Hormann and Brandt (2007) pointed out strong correlations between the interannual variability of the EUC and the South Equatorial Current (SEC) west of 10°W, and SST in the eastern Atlantic Cold Tongue (ACT) during the boreal summer. The anomalous cold (warm) SST in the ACT is associated with a stronger (weaker) EUC and SEC transports west of 10°W. However, Hormann and Brandt (2007) did not address explicitly the interannual variability of the EUC east of 10°W, and observations were until recently too sparse to document it.

In this paper, observations from recent oceanographic cruises, during which simultaneous measurements of currents and hydrology were obtained along meridional sections between 10°W and 6°E, are analyzed to describe the fate and seasonal variability of the EUC and its associated salinity maximum in the Gulf of Guinea (GG; defined here as the region extending from 15°S to 5°N and from 15°W to 15°E). These measurements are complemented by observations from PIRATA moorings and from ARGO profiling floats, and by a high-resolution Ocean General Circulation Model (OGCM) simulation of the tropical Atlantic Ocean. Section 2 describes the data and the model used in this study. Section 3 focuses on observations carried out in June 2007. In Sect. 4, the seasonal evolution of the salinity maximum associated with the EUC from boreal spring to fall is addressed from observations. In Sect. 5, the observations are compared with the numerical simulation, and explained in the light of the seasonal cycle of the EUC termination. The main results are discussed in the last section.

2 Observations and model

2.1 Data

2.1.1 Cruises

The data used in this study were collected in the Gulf of Guinea in 2000 during EQUALANT-2000 cruise (Bourlès

Table 1 Description of the different cruises

Cruises	year	Longitude	Date	SADCP (kHz)	Vessel
EQUALANT 2000	2000	10°W	31 July	75	La Thalassa
		0°E	9 August		
		6°E	14 August		
EGEE 1	2005	10°W	10 June	150	Le Suroît
		2.8°E	26 June		
EGEE 2	2005	10°W	13 September	150	Le Suroît
		2.8°E	22 September		
		6°E	27 September		
EGEE 3	2006	10°W	2 June	75	L'Atalante
		2.5°E	15 June		
		6°E	21 June		
EGEE 4	2006	10°W	21 November	75	L'Antéa
		2.4°E	29 November		
EGEE 5	2007	10°W	30 June	75	L'Antéa
		2.3°E	14 June		
		6°E	8 June		
EGEE 6	2007	10°W	23 September	75	L'Antéa
		0°E	11 September		
		6°E	5 September		

The date of each section refers to the date of the station at the equator

et al. 2002), and from 2005 to 2007 during 6 repetitive cruises in the framework of EGEE (Etude de la circulation océanique et des échanges océan-atmosphère dans le Golfe de Guinée) (Bourlès et al. 2007) as part of the AMMA (African Monsoon Multidisciplinary Analysis) program (Redelsperger et al. 2006). Details about these cruises are given in Table 1.

During these cruises, 19 meridional hydrological sections, including measurements of zonal and meridional currents from Ship-mounted Acoustic Doppler Current Profilers (SADCP), were carried out along 10°W, near 2°E and along 6°E. Temperature, salinity and dissolved oxygen measurements were collected from CTD-O_2 SeaBird probes along each section at a spatial resolution of at least 0.5° in latitude. En-route SADCP measurements cover the depth range from 20 m down to about 150 m (EGEE1 and EGEE2) or 350 m (other cruises). Absolute referencing was provided by Global Positioning System (GPS) navigation. SADCP data were first hourly-averaged, then linearly interpolated onto a regular grid with a resolution of 0.1° in latitude and 1 m in depth. The standard error of the hourly-averaged velocities, $S_E = STD/\sqrt{N}$ (estimated as the STD of the hourly mean velocity divided by square root of the sample size, *N,* i.e. the number of data used in the hourly mean estimates), is around 1 cm s^{-1} on average for each cruise.

For validation purpose, we also used the velocity and hydrographic data of 17 historical cruises carried out at 10°W between 1997 and 2007 and described in Kolodziejczyk et al. (2009). Note that the 10°W sections from EQUALANT-2000 and EGEE 1-to-6 are common to the present paper and Kolodziejczyk et al. (2009). These data allow a validation of the mean sections of zonal velocity and salinity at 10°W, and of the seasonal cycle of the transport at 10°W estimated with the model output.

2.1.2 *PIRATA moorings*

In the framework of the PIRATA program (Bourlès et al. 2008), 2 meteo-oceanic moorings are maintained since 1997 along the equator in the eastern Atlantic, namely at 10°W and 0°E. These moorings provide daily time series of temperature at 11 depth levels from the surface down to 500 m depth, with a 20 m resolution from the surface down to 140 m depth; and of salinity at 6 levels from surface to 120 m depth with a 20 m resolution. The mean seasonal cycles of temperature and salinity were calculated for each PIRATA buoy location and for each depth from the complete time series (covering the period September 1997–August 2013). The data sets suffer from numerous gaps (refer to http://www.brest.ird.fr/pirata/ for details on the PIRATA datasets), but at least 7 complete years of temperature and salinity data were available at most depths at 10°W and 0°E. Note however that there is only about 1 year of salinity measurements at 60 m (at 10°W and 0°E) and at 80 m (at 0°E), and no salinity data at 80 m at 10°W. In particular, there is no salinity measurement at these depths in June–August at 10°W and in April at 0°E.

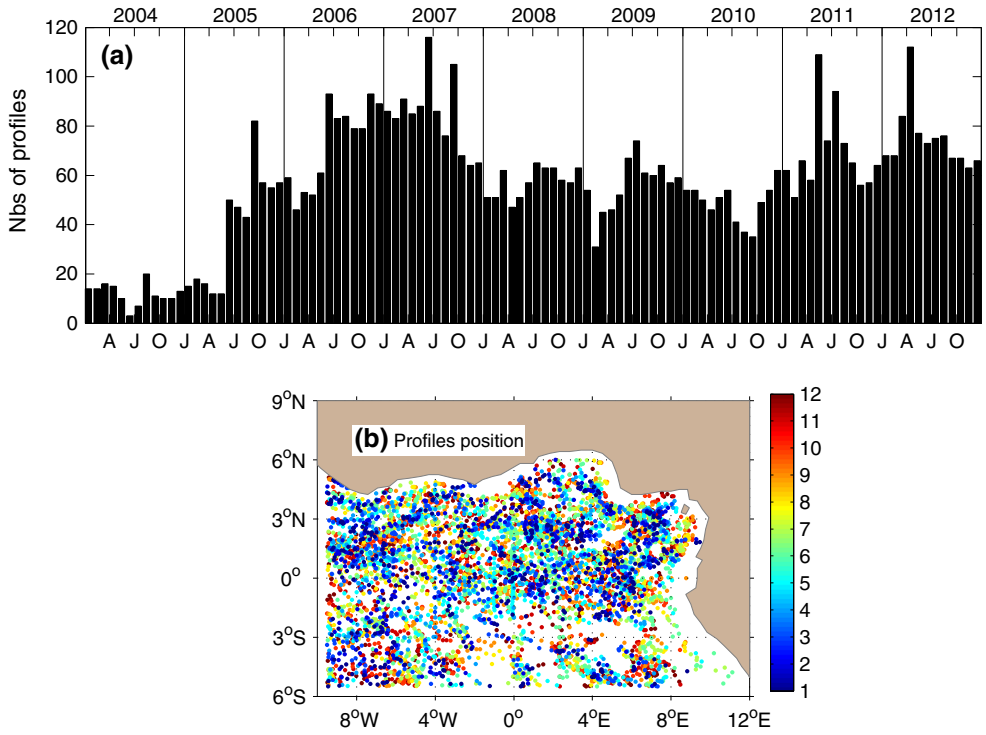

Fig. 1 **a** Number of Argo T-S profiles in the Gulf of Guinea (6°S–N–8°W–12°E) as a function of time between 2004–2012 (in month). **b** Monthly distribution of Argo profiles in the Gulf of Guinea for the period 2004–2012

2.1.3 Argo floats

The hydrological profiles from Argo floats used in this study have been downloaded from the Coriolis Data Center (http://www.coriolis.eu.org/). A climatological test was applied to the data set, and followed by a visual control of suspicious profiles in the framework of the "*Global Ocean Surface Salinity Calibration and Validation*" (GLOSCAL) project (Gaillard et al. 2009). The individual profiles available in the GG between 2004 and 2012 provide a spatial and monthly coverage since mid-2005 (more than 50 profiles per month) that is expected to be large enough to describe the seasonal variability of the temperature and salinity in this region (Fig. 1; see also Wade et al. 2011).

2.2 Model description and validation

2.2.1 NEMO model

In this study, we use the numerical outputs of a Tropical Atlantic configuration (30°S–30°N) of the Ocean General Circulation Model NEMO 3.1 (Madec 2008). This configuration is similar to the DRAKKAR experiment (Barnier et al. 2006). The horizontal resolution is 1/4° and there are 46 vertical levels (16 levels within the first 300 m and 10 levels in the first 100 m). This configuration is forced at its meridional boundaries (30°N–S) and its western boundary (60°W) by the 5-day outputs of the global ORCA025-G85 simulation (Barnier et al. 2006), using the "mixed" open boundary algorithm (Barnier et al. 1998; Tréguier et al. 2001).

For the purpose of this study, the model includes a high-resolution sub-domain (1/12° horizontal resolution and same vertical grid) between 10.7°W and 14.5°E and between 13.7°S and 7.5°N, through the 2-way Adaptive Grid Refinement In Fortran (AGRIF; www.nemo-ocean.eu) module of the NEMO 3.1 code. This gain of resolution in the GG allows a better representation of the fine structures of the surface and subsurface, like river plumes characterized by sharp Sea Surface Salinity (SSS) fronts that could impact the SEC and EUC circulation and water masses in the eastern GG. The boundary conditions of the AGRIF sub-domain region are provided by the larger-scale model at each time step.

The model is forced with the atmospheric fluxes of momentum, heat and freshwater provided by DRAKKAR Forcing Set 4.3 (DFS 4.3) (Brodeau et al. 2010). This dataset is a combination of ECMWF-ERA40 (European Centre for Medium-Range Weather Forecasts) 6-hourly reanalysis and observations. Radiative fluxes are provided by daily satellite measurements, while precipitations come from monthly satellite measurements. The evaporation minus precipitation (E-P) flux includes a relaxation to climatological E-P with a coefficient of -56 mm day^{-1} PSS^{-1}. The rivers' runoffs

are provided by the monthly climatology of Dai and Trenberth (2002).

The vertical turbulent mixing is parameterized using a TKE scheme (Blanke and Delecluse 1993) with a background vertical diffusivity coefficient equal to 10^{-6} m^2 s^{-1}. Since convective mixing due to static instability cannot be represented in hydrostatic models, a TKE source is added in case of density inversion in the mixed-layer with an enhanced background vertical diffusivity coefficient set to 10^{-4} m^2 s^{-1}. In the GG sub-domain (1/12° resolution), the horizontal friction scheme is bilaplacian, applying on horizontal surfaces with a friction coefficient equal to -1.25×10^{11} m^4 s^{-1}, while diffusion is isopycnal and laplacian with a diffusion coefficient equal to 100 m^2 s^{-1}.

The monthly-averaged and 5-day-averaged outputs of the simulation for the period 1993–2007 are used in this study. The model is started from rest on 1 January 1990. The initial conditions for temperature and salinity were derived from the World Ocean Atlas climatology (Antonov et al. 2010; Locarnini et al. 2010). Only model outputs after 1993 (i.e. after 3 years of spin-up) are considered.

The present study will mostly focus of the main properties and transports within the upper thermocline (defined as the within the $\sigma_\theta = 24.5$–26.2 isopycnal layer), where the EUC core and the associated salinity maximum lie, or within the thermocline (defined as the within the $\sigma_\theta = 24.5$–26.5 isopycnal layer), where most of the EUC transport takes place. For each 5-day output of the model, we first determine the depths of the two isopycnals from the linear interpolation of the vertical density profile at each gridpoint, and then average (for mean fields) or integrate (for transports) the model fields between these two depths (taking into account the thickness of the vertical grid cells). We checked that the 24.5, 26.2 and 26.5 isopycnals never outcrop in the eastern equatorial Atlantic.

2.2.2 *Model validation*

2.2.2.1 Mean EUC Numerical results are compared with available sections from cruises (see Tables 1 and 2) and PIRATA moorings measurements. In order to validate the mean state of the model, meridional sections of zonal velocity and salinity at 10°W from the model and from the observations described by Kolodziejczyk et al. (2009) have been compared. It is worth noting that there were no observations at 10°W during boreal spring in Kolodziejczyk et al. (2009), so the mean sections from observations might be biased. In order to compare consistently the model with the time-average of observations from sparse sections (Fig. 2), we computed the time-averaged sections in the model from outputs both over the complete 1993–2007 period and at the same dates as the 17 available sections. We note that the two different ways of averaging in the model give comparable meridional sections in zonal velocity (Fig. 2a, c) and in salinity (Fig. 2b, d) at 10°W, indicating that an average over the 17 available synoptic cruises is able to capture the main properties of the circulation and of the salinity at 10°W.

Table 2 Total (0–250 m) and upper thermocline ($\sigma_\theta = 24.5$–26.5) EUC transports across the meridional sections of the different cruises used in this study (Unit is Sv)

Date	Section	Total Transport (Sv)	$\sigma_\theta = 24.5$–26.5 Transport (Sv)
31 July 2000	10°W	20.0	12.8
10 June 2005	10°W	20.2	14.6
13 September 2005	10°W	17.4	12.1
2 June 2006	10°W	24.4	14.6
21 November 2006	10°W	9.6	9.0
30 June 2007	10°W	9.3	8.3
23 September 2007	10°W	27.3	17.1
26 June 2005	2.8°E	11.3	8.9
22 September 2005	2.8°E	12.6	9.3
15 June 2006	2.5°E	4.3	…
29 November 2006	2.4°E	11.8	9.7
14 June 2007	2.3°E	15.2	11.6
9 August 2000	0°E	11.1	5.9
11 September 2007	0°E	11.8	10.4
14 August 2000	6°E	0.0	0.0
27 September 2005	6°E	4.4	3.8
21 June 2006	6°E	1.7	1.5
8 June 2007	6°E	6.7	4.4
5 September 2007	6°E	5,6	4.3

In both model and observations, the mean EUC core at 10°W is located at 0.2°S around 70 m depth, within the $\sigma_\theta = 24.5$–26.2 isopycnal layer (Fig. 2c, e); the EUC has a larger extent in latitude in the southern hemisphere (as far as 2°S around 50 m depth) and it extends down to at least 250 m depth. The simulated EUC has greater maximum speed (88 cm s^{-1}) than in observations (69 cm s^{-1}), and its associated eastward velocities meridional distribution is narrower below 100 m depth. The SEC is also well comparable in model and observations, with maximum westward velocities of about 30 cm s^{-1} near the surface, two deep branches of westward velocities centered at about 3°S and 2°N down to at least 300 m and a subsurface maximum (>10 cm s^{-1}) in the northern deep branch of the SEC at 2°N around 100 m depth. The Guinea Current (GC) is also present in the model, flowing eastward above 50 m depth north of 2.5°N (Richardson and Reverdin 1987). Unfortunately, there were no observations north of 2°N to validate the model results from 2°N to the African coast.

Following Kolodziejczyk et al. (2009), two estimates of the EUC transport are computed from the model and from

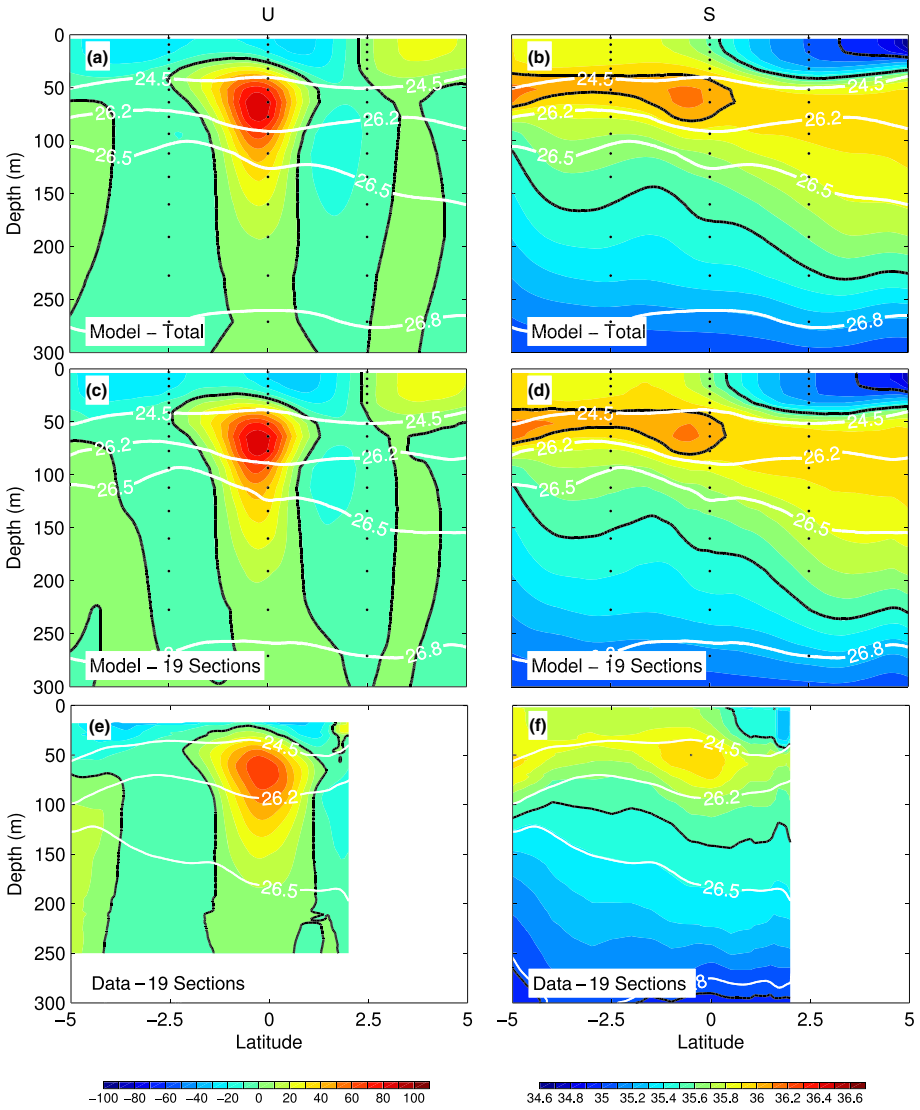

Fig. 2 Mean meridional sections at 10°W of zonal currents (*left*) and salinity (*right*) in the model (**a**–**d**) and from observations (**e**–**f**) (Kolodziejczyk et al. 2009; their Table 2). To facilitate the comparison with the observations, the time-averaged sections from the model have been computed from the full 1993–2007 period (**a**, **b**) and from the outputs at the same dates as the 17 hydrographical sections in Kolodziejczyk et al. (2009) (**c**, **d**). Currents are in cm s^{-1}. *Thick black lines* refer to the zero isotach in (**a**), (**c**) and (**e**), and to 35.0, 35.5 and 36.0 isohalines in (**b**), (**d**) and (**f**). Isopycnals 24.5, 26.2, 26.5 and 26.8 are superimposed in *solid white lines*. *Black dots* in (**a**–**d**) represent the vertical grid of the model

the observations (Table 2). They are defined as the integral of eastward velocities between 2.5°S and 2°N, either in the $\sigma_\theta = 24.5$–26.5 density range (*thermocline EUC transport*) or in the 0–250 m depth range (*total EUC transport*), for all cruises but EGEE1 and 2 cruises during which the total EUC transport was computed only between the surface and 150 m due to the limited S-ADCP depth range (see Kolodziejczyk et al. 2009).

Despite the stronger velocity maximum in the model, the mean total EUC transports at 10°W are comparable in both the model (12.7 ± 7.4 Sv from individual sections; 12.8 ± 7.4 Sv with the full 15-year time series) and observations (12.1 ± 1.9 Sv), as well as the thermocline EUC transports from observations (8.9 ± 0.8 Sv) and from the model (8.9 ± 3.6 Sv from individual sections; 9.3 ± 3.8 Sv with the full 15-year time series). For the total EUC transport, this can be explained by the smaller meridional extent of the EUC below 100 m in the model. For the thermocline EUC transport, this results from the smaller thickness of the thermocline layer in the model, due to the greater mean depth of the $\sigma_\theta = 26.5$ isopycnal at the equator in the observations (170 m) than in the model (130 m), so that the thermocline layer ($\sigma_\theta = 24.5$–26.5 density range) encompasses a larger portion of the EUC in the observations (Fig. 2c, e). It is worth mentioning that the stratification below the thermocline appears to be more diffuse in the model than in the in situ data.

The salinity maximum associated with the EUC core reaches 36.18 in the model, and 36.00 PSS in the observations (Fig. 2d, f). This positive bias around 0.18 PSS in the model is found to occur over the whole $\sigma_\theta = 24.5$–26.5 isopycnal range between 5°S and 2°N, indicating that salinities are generally too strong in the simulated equatorial thermocline. Nevertheless, the mean latitudinal distribution of salinity within the upper thermocline agrees qualitatively in the model and in the observations. Both

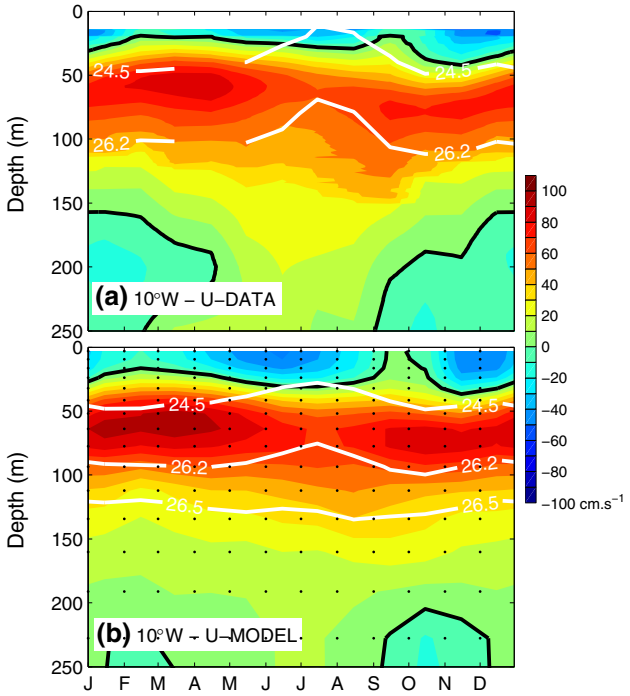

Fig. 3 Climatological Month-depth evolution of the zonal velocities (in cm s^{-1}) between 0–250 m depth at 0°N–10°W (**a**) from available currentmeters data between 2003 and 2007, and (**b**) from NEMO model output between 1993 and 2007. Isopycnals 24.5, 26.2, and 26.5 are superimposed in *solid white lines*. *Black dots* in (**b**) represent the vertical grid of the model

sections show (i) a well-defined salinity maximum associated with the EUC core in the upper thermocline layer ($\sigma_\theta = 24.5$–26.2) slightly south of the equator, (ii) stronger salinities along the $\sigma_\theta = 24.5$ isopycnal in the southern hemisphere than north of the equator, (iii) the presence of a second salinity maximum around 50 m depth along the $\sigma_\theta = 24.5$ isopycnal south of 4°S, which is the signature of subtropical waters originating from the southern hemisphere (Kolodziejczyk et al. 2009), and (iv) a sharp halocline around 40 m depth in the northern hemisphere, with surface salinities lower than 35.4 PSS.

2.2.2.2 *Seasonal variability at the equator*

(a) Zonal velocity

In the Atlantic Ocean, the EUC exhibits a robust seasonal cycle between 35°W and 0°E both in observations (e.g., Brandt et al. 2006; Kolodziejczyk et al. 2009; Johns et al. 2014) and in models (e.g., Arhan et al. 2006). In order to get more insight into the ability of our model to reproduce the seasonal variability of EUC velocities, we compare the mean seasonal cycle of equatorial zonal velocities at 10°W in the model (Fig. 3b) with the mean seasonal cycle derived from ADCP measurements from the PIRATA mooring between June 2003 and December 2007 (Fig. 3a). The ADCP measurements suffer from one important gap between June 2005 and May 2006, and were available only in the first 100 m in 2006–2007. However, the period of PIRATA observations encompasses at least 3 complete years in the upper 100 m, which is likely enough to capture the predominant features of the seasonal cycle.

In the upper 100 m, the zonal velocities are generally stronger (of about 10–20 cm s^{-1}) in the model than in the PIRATA mooring, while they are somewhat less intense below 150 m. However, the seasonal evolution and vertical structure of the zonal velocities are qualitatively reproduced in the model: (i) the depth of the EUC core ranges between 50 and 70 m depth, shallowing during the boreal winter and spring and deepening in summer and fall; (ii) the EUC core is encompassed throughout the year in the upper thermocline, between $\sigma_\theta = 24.5$ and $\sigma_\theta = 26.2$ isopycnals; (iii) above 50 m depth, the eastward velocities associated with the EUC extend upward to the surface during September, in agreement with the annual weakening/reversal of the SEC (Ding et al. 2009); (iv) below 150 m depth, an annual reversal of the zonal current is found (though of lesser amplitude in the model), with predominantly eastward velocities from April to September and westward velocities from October to March.

(b) Salinity and temperature

Then, we compare the mean seasonal variability of the salinity maximum computed with the model (Fig. 4c, d) and computed from PIRATA moorings data at 10°W–0°N and 0°E–0°N between 1998 and 2012 (Bourlès et al. 2008; Fig. 4a, b).

At both longitudes the salinity seasonal cycle is qualitatively well reproduced in the model: (i) the salinity maximum associated with the EUC is present between 40 and 80 m, and is located throughout the year between the $\sigma_\theta = 24.5$ and $\sigma_\theta = 26.2$ isopycnals; (ii) the strong annual cycle in surface salinity, and in the vertical gradient of salinity between the surface and 50 m depth, is comparable in the model and in the observations, with weakest values in February–May and strongest values in boreal summer and fall. (iii) this salinity maximum is subject to a semi-annual variability, with maximum salinity in April and October–November, but the intense weakening of the salinity maximum in December at 10°W is not reproduced in the model. However, as previously noted in the mean salinity section at 10°W, there is a constant bias in salinity in the model, the simulated salinity of the upper layer of the equatorial GG being about 0.2 PSS saltier than the observed one. This constant bias however does not affect the seasonal variability of near-surface salinities in the model.

The seasonal cycles of temperature at 10°W and 0°E in the model (Fig. 5c, d) also display a qualitative good

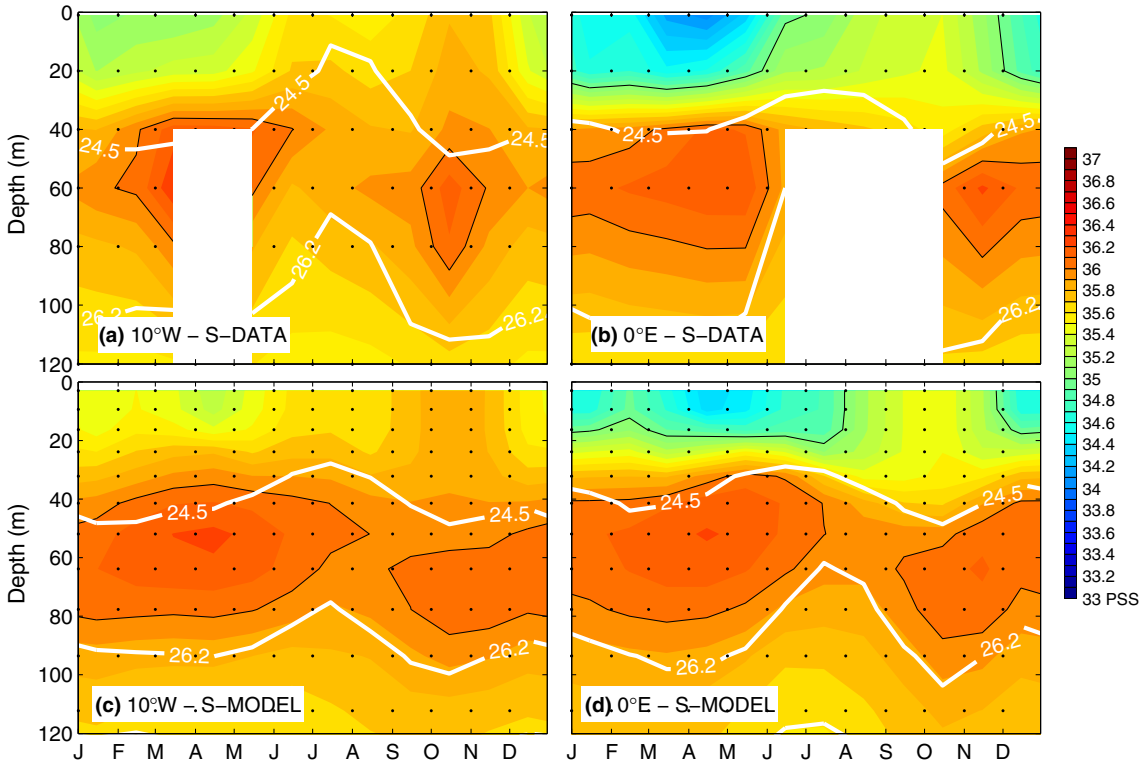

Fig. 4 Climatological Month-depth evolution of the salinity (in PSS) between 0–120 m depth (**a**, **b**) from available PIRATA salinity data between 1998 and 2013 and (**c**, **d**) from NEMO model output between 1993 and 2007, at 0°N–10°W (**a**–**c**) and 0°N–0°E (**b**–**d**). Isopycnals 24.5 and 26.2 are superimposed in *solid white lines*. *Black dots* in (**c**, **d**) represent the vertical grid of the model

agreement with the seasonal cycles derived from PIRATA moorings at 10°W and 0°E (Fig. 5a, b): (i) the 20 °C isotherm is located around 70 m depth during boreal winter–spring and 40–50 m depth during the boreal summer; (ii) the depth of the thermocline experienced a clear semi-annual cycle, being shallower during late boreal spring and summer, and with a lesser amplitude in December at both longitudes; (iii) the 24.5–26.2 isopycnal layer encompasses the strongest vertical gradient of temperature of the upper thermocline throughout the year; (iv) at 0°E, the thermocline is sharper during boreal summer in both data and model.

As for the zonal velocities, the model thus reproduces qualitatively well the observed water masses properties, their vertical distribution and their seasonal variability in the upper layers at 0°N–10°W and 0°N–0°E.

(c) EUC transport

To assess the ability of the model to reproduce realistic EUC transports in the eastern Atlantic ocean, Fig. 6 presents scatter plots of the total and thermocline EUC transports estimated from the available synoptic meridional sections over the period 1999–2007 at 10°W, ∼1°E and 6°E, and the corresponding estimates from the model at the same longitudes and dates. At 10°W and 1°E, the total (Fig. 6a) and thermocline (Fig. 6b) EUC transports are reasonably simulated for the values that are close to the mean values (squares), i.e. for transports between 5 and 20 Sv. Nevertheless, the largest total and thermocline EUC transports in the observations (beyond 20 Sv at 10°W and 12 Sv at ∼1°E, respectively) are systematically lower in the model. Along 6°E (red circles), the EUC transports are generally too intense in the model.

To put these estimates for the EUC transport in the context of the seasonal variability, Fig. 7 presents the mean monthly evolution of the total and thermocline EUC transports (solid), their standard deviation (STD; gray shaded) and their maximum/minimum (dashed lines) in the model, along with the corresponding estimates from available observations (black dots), at 10°W, 1°E and 6°E. The standard deviation, the minimum and maximum of EUC transports have been computed for each calendar month from the 5-day outputs of the model over the period 1993–2007.

At 10°W (Fig. 7a, b), 17 different estimates of the EUC transport spanning the whole year are available from Kolodziejczyk et al. (2009) (see their Table 2 for more details). Note however that most cruises took place from June to September and from November to February, with only one estimate for the total EUC transport during boreal

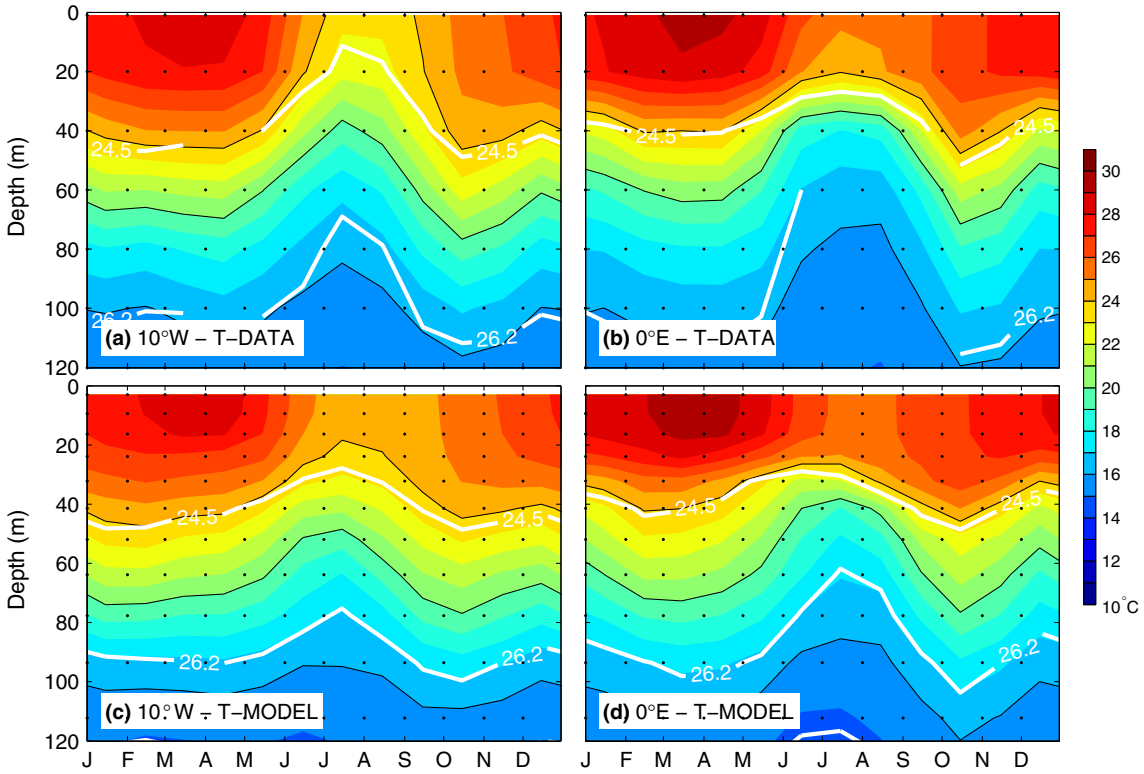

Fig. 5 Same as Fig. 4, except for temperature

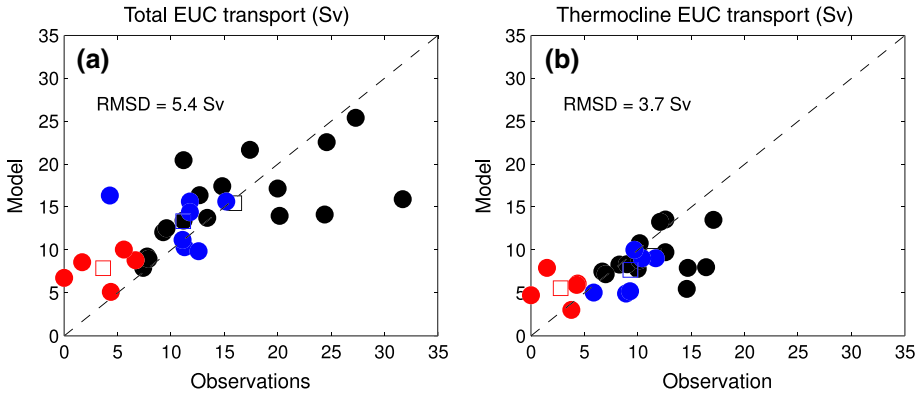

Fig. 6 Comparison of the individual **a** total and **b** thermocline ($\sigma_\theta = 24.5$–26.5) EUC transports estimated from the different cruises and from the model, at 10°W (*black dots*), 0°E (*blue dots*) and 6°E (*red dots*). Cruises are described in Kolodziejczyk et al. (2009) and in Table 2. The *squares* represent the mean values at each longitude. The Total Root Mean Square Deviation (RMSD) and linear fit (*dashed line*) are indicated in each sub-figure

spring (no CTD data during this cruise) and no observation in October. The observations and the model indicate a yearly maximum of both total and thermocline EUC transports in August–September and a yearly minimum during November–December, as confirmed from moored current-meters by Johns et al. (2014). The model further exhibits a very weak maximum during the boreal spring that agrees with the observations by Johns et al. (2014), but cannot be evidenced from the unique synoptic section available during this season. The transport estimates from observations exhibit a maximum range of variability during boreal summer and a minimum range during November–December that roughly agree with the minimum/maximum transports computed from the 5-day model output (Fig. 7). The cruise-to-cruise variability is lower in boreal fall and winter than during boreal summer, suggesting less intra-seasonal or interannual variability of the EUC transport during this period.

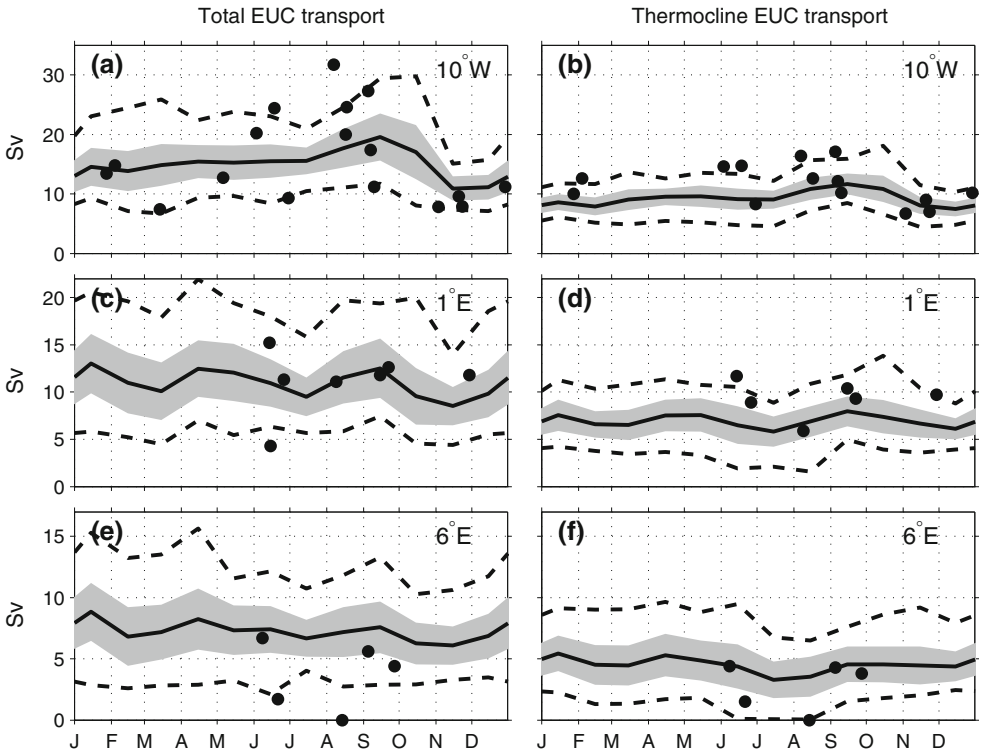

Fig. 7 Seasonal variability of the EUC transport (in Sv) in the model: total transport (0–250 m) (*left*) and thermocline transport (σ_θ = 24.5–26.5) (*right*), at 10°W (*upper*), 1°E (*middle*) and 6°E (*lower*). *Black curves* represent the monthly mean transport, during the period 1993–2007. Standard deviation for the monthly transports (calculated from the 5-day output) is superimposed in gray. *Dashed lines* refer to maximum and minimum values taken from the 5-day output for each month. *Circles* represent the individual estimates from observations in Kolodziejczyk et al. (2009) (their Table 2) and in this study (Table 2)

At 1°E and 6°E (Fig. 7c–f), observations are available only from June to November, and in limited number. For this period, both model and observations indicate that the total and thermocline EUC transports weaken from 10°W to 6°E (Fig. 6b, d, f). Note in particular that the transport almost vanishes at 6°E during one cruise in August 2000 (see also Bourlès et al. 2002). Moreover, in agreement with observations by Johns et al. (2014), the total and thermocline EUC transports in the model exhibit a seasonal maximum in April at 1°E, but no cruise is available during this season.

3 Evidence of a westward recirculation of the EUC salinity maximum in June 2007

In this section, we focus on the observations of currents, salinity and dissolved oxygen acquired in June 2007 in the Gulf of Guinea during the EGEE5 cruise (Fig. 8). The meridional sections of salinity along 10°W, 2.3°E and 6°E (Fig. 8d–f) reveal, within the upper thermocline layer (defined here between the 24.5 and 26.2 isopycnals), the presence of high salinities (exceeding 36.0) both at the equator and off the equator (near 3°N and 3°S at 2.3°E), as previously evidenced by Gouriou and Reverdin (1992). At the equator, high salinities are observed along the three sections at the depth of the EUC core (Fig. 8d–f) and coincide with high dissolved oxygen concentrations (up to 120 µmol kg^{-1}; Fig. 8g–i). At 10°W, it is worth noticing that the strong salinities that are visible south of 4.5°S around the 24.5 isopycnal (Fig. 8a, d), in the region of the eastward South Equatorial Undercurrent (SEUC) do not result from the recirculation of the EUC in the eastern GG. They are likely the signature of the subtropical water masses from the south Atlantic advected by the SEUC (Kolodziejczyk et al. 2009), and are thus beyond the scope of the present study.

The EUC maximum velocity decreases eastward from 70 cm s^{-1} to 40 cm s^{-1} (Fig. 8d–f), while the thermocline EUC transport first increases from 8.3 Sv to 11.6 Sv between 10°W and 2.3°E, and subsequently decreases to 4.4 Sv at 6°E. Note that both eastward velocities and high oxygen concentrations extend below σ_θ = 26.2 (down to the 26.5 isopycnal) at 10°W and 2.3°E, i.e. deeper than the salinity maximum of the EUC core which is confined to the upper thermocline (Fig. 8d, g).

At 6°E, salinities exceeding 35.9 and dissolved oxygen concentrations greater than 150 µmol kg^{-1} cover the whole latitude range of the meridional section (between 1°S to 2.5°N) in the upper thermocline (Fig. 8i), in contrast with the EUC that remains confined between 1°N and 1°S (Fig. 8c). Between 1°N and 2.5°N, high salinities are associated with a westward current, which strongly suggests that EUC water masses spread poleward and recirculate westward near that longitude.

At 2.3°E, this extra-equatorial westward recirculation of EUC water masses is more clearly identified through the presence of two maxima of salinity (up to 36.2) and oxygen

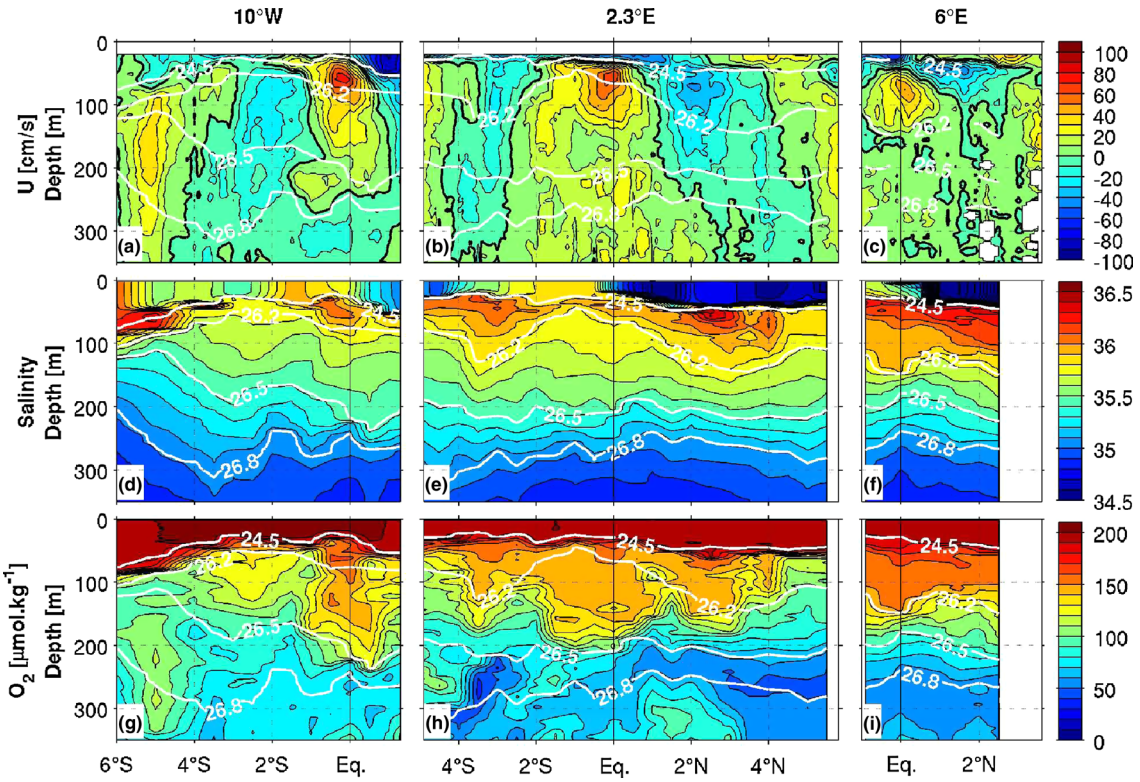

Fig. 8 Meridional sections at 10°W (*left column*), 2.3°E (*central column*) and 6°E (*right column*) of zonal velocity (*upper*; in cm s^{-1}; isotach 0 in *bold*), salinity (*middle*) and dissolved oxygen (*lower*; in µmol kg^{-1}) as measured during the EGEE5 cruise in June 2007. Isopycnals 24.5, 26.2, 26.5 and 26.8 are superimposed in *solid white lines*

(140 µmol kg^{-1}) near 3°S and 3°N, with values comparable with those at 6°E. Contrary to 6°E, the high salinity cores off the equator are clearly distinct from the equatorial salinity maximum related to the EUC core (Fig. 8e). The total transports of these westward flows within the upper thermocline are 5.5 and 2.0 Sv respectively north and south of the equator, leading to a total extra-equatorial westward transport of 7.5 Sv in the upper thermocline. These results are comparable with the observations made in March 1995 at 3°E by Mercier et al. (2003).

At 10°W, a westward current is still found in the thermocline between 1°S and 3°S (Fig. 8a). This current is still associated with a relative maximum of oxygen (up to 120 µmol kg^{-1}), but no longer with a local salinity maximum. However, the horizontal distribution of salinity and oxygen in the upper thermocline at 2.3°E and 10°W around 3°S strongly suggests the continuity of the westward extra-equatorial circulations of saline water masses originating from the EUC.

4 Seasonal variability of the upper EUC water masses

We now focus on the time evolution of vertical average of salinity and the zonal transport in the upper thermocline (σ_θ = 24.5–26.2 isopycnal range)—i.e. where the salinity maximum associated with the EUC core is confined—as observed from all the individual Argo profiles available from 2004 to 2012 (Fig. 9) and seven cruises available from June to November between 2000 and 2007 (Fig. 10).

In the GG, the coverage of Argo profiles is sufficient to depict the climatological seasonal variability of the mean salinity within the upper thermocline (Fig. 9). In spite of possible intra-seasonal and inter-annual variability in the data, a robust seasonal cycle is observed. From January–February to May–June (Fig. 9a–c), the upper thermocline is characterized by a tongue of high saline water masses (up to 36.1 PSS) along the equator (within a ±1.5° latitude band) extending over the whole GG. In the eastern GG, these saline water masses progressively spread off the equator, and westward along 3°N–S until May–June. During July–August (Fig. 9d), the mean salinity in the upper thermocline dramatically weakens down to 35.7 PSS along the equator, while the extra equatorial maxima of salinity remain present east of 0°E. From September–October (Fig. 9e–f), the equatorial salinity maximum first reforms west of 0°E, before extending again over the whole GG in November–December (Fig. 9f), while the extra-equatorial maxima progressively disappear during this season.

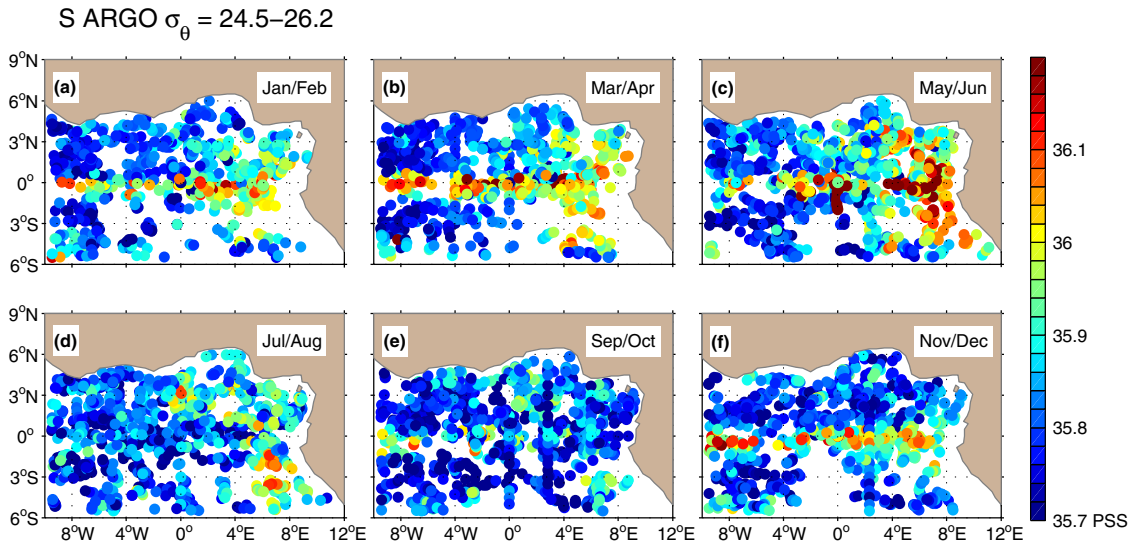

Fig. 9 Bi-monthly climatology of mean upper thermocline salinity (*shaded color*; in PSS) from each available Argo profiles in the GG between 2004 and 2012. Months from January/February (**a**) to November/December (**f**) are indicated in each subfigure

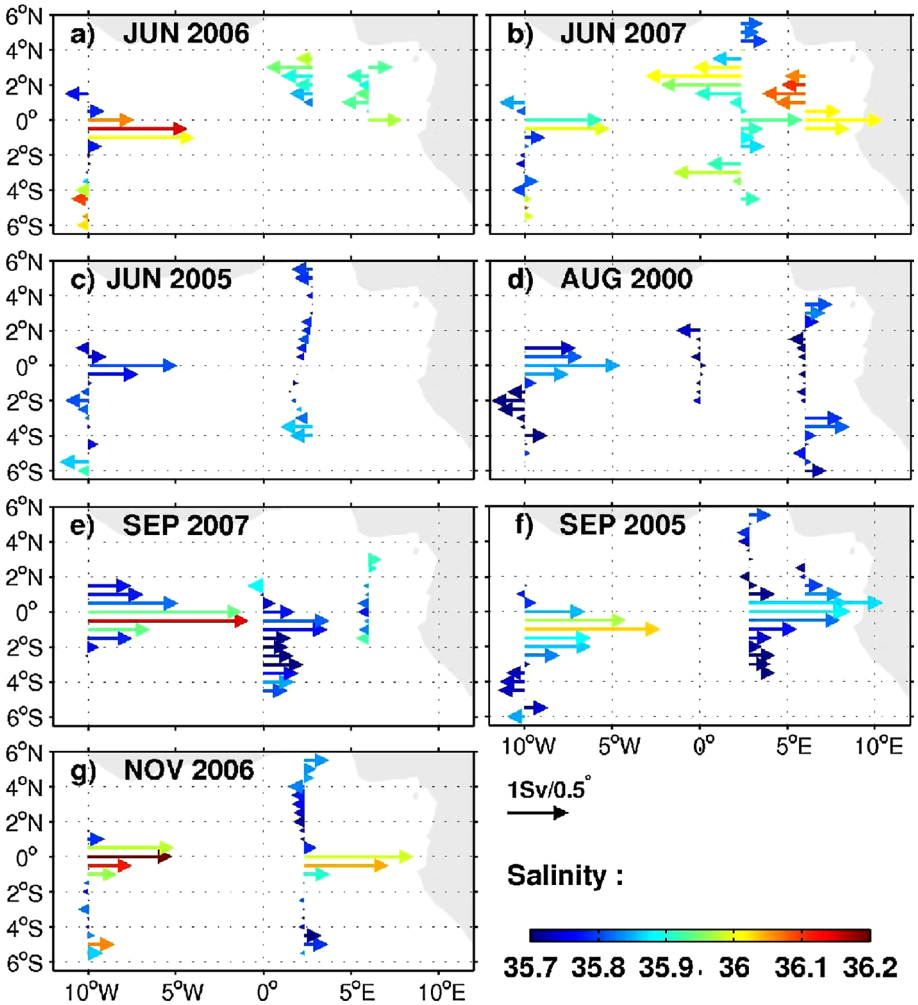

Fig. 10 Zonal transport per 0.5° of latitude (*arrows*; in Sv) and mean salinity (*color*; in PSS) in the upper thermocline (24.5–26.2 isopycnal layer) during each cruise. The month and year of each cruise are indicated in each subfigure. *Scaling* for transport and salinity is provided in the bottom/right

The seven cruises carried out in the GG between 2000 and 2007 allow us to describe the salinity and the associated horizontal transport distribution during the summer to fall season. During June 2006 and 2007, the year-to-year distribution of salinity and transport presents qualitatively common features (Fig. 9a, b), *e.g.* the EUC is observed along the equator from 10°W to 6°E with salinities greater than 35.9. As described in the previous section, westward recirculations are observed north and south of the equator in June 2007 at 2.3°E and north of the equator at 6°E, transporting salty waters with comparable salinity values as for the EUC at the equator (Fig. 9b). A similar recirculation is suggested north of the equator across 6°E and 2.5°E in June 2006 (Fig. 10a), but there is no data for this cruise to confirm its existence in the southern hemisphere. During June 2006 and 2007, the salinity distribution agrees qualitatively well with the seasonal one given from Argo data (Fig. 9c).

Nevertheless, during June 2005 and August 2000 (Fig. 10c, d), the salinity distribution clearly differ from the seasonal picture given from Argo data during May–June (Fig. 9c) and July–August (Fig. 9d), whereas the horizontal distribution of transports are alike during June 2005 and August 2000. During both cruises, the EUC is only present at 10°W, but the associated salinity maximum is weaker than the corresponding bi-monthly distribution suggested in Argo data. At 2.3°E (in June 2005) and 0°E (in August 2000), zonal transports at the equator are weak, even westward, suggesting that the upper EUC does not penetrate in the eastern GG during these two cruises. In June 2005 at 2.3°E, extra-equatorial salinity maxima are weaker than the ones obtained in May–June from Argo data, and associated with weak westward transports. In August 2000 at 6°E, weak extra-equatorial salinity maxima are observed on both sides of the equator near 3°S and 3°N, associated with eastward flows. The June 2005 and August 2000 cruises data strongly suggest that interannual variability may strongly modulate the mean seasonal variability deduced from Argo measurements.

In September 2005 and 2007 and November 2006 (Fig. 9e–g), the EUC is again observed in the upper thermocline with a high salinity signature, in agreement with salinity Argo distribution during this year period (Fig. 9e, f). In early September (2007; Table 1), the upper EUC does not reach 6°E and salinity is weaker than 35.8 near 0°E (Fig. 10e). In contrast, in late September (2005; Table 1), the EUC is present from 10°W to 6°E, and carries salinity of about 35.9 at 2.3°E and 6°E (Fig. 9f). In November 2006 (Fig. 10g), the EUC is associated with salinities greater than 36.0 at 2.3°E. This suggests a progressive eastward penetration of the EUC and saline water masses along the equator from late boreal summer to mid boreal fall, thus supplying again the GG with high salinity waters of subtropical origin. In agreement with Argo data, neither salinity maximum nor intense westward recirculations are observed off the equator during these three cruises.

5 Seasonal variability of the EUC termination in the model

5.1 EUC termination and circulation of saline water masses

To infer in more details the horizontal structure of the upper thermocline circulation in the GG and overview its complete seasonal cycle, we now analyze the bi-monthly climatological horizontal distribution of mean salinity and transports within the upper thermocline, calculated from the 1993–2007 NEMO simulation (Fig. 11).

From May to November (Fig. 11c–f), the seasonal evolutions of zonal transport and salinity in the upper thermocline are qualitatively in good agreement with the descriptions provided in the previous section: (i) the EUC slightly weakens from May, then strongly diminishes and disappears east of 5°E during July–August (Fig. 11c–d). It strengthens in September–October when it is present again until the African coast (Fig. 11e); (ii) extra-equatorial westward transport are intensified between 2° and 3° in both hemispheres from May to July (Fig. 11c–d); (iii) a strong salinity maximum is present near the equator in May–June (Fig. 11c), is largely eroded in July–August (Fig. 11d) and reappears from the west in September (Fig. 11e); (iv) extra-equatorial salinity maxima are observed from May to August near 3°N and 3°S (Fig. 11c, d). These extra-equatorial high salinities are spatially connected to the EUC salinity maximum in May–June in the eastern half of the GG (Fig. 11c). Then they persist in time, despite the disappearance of the EUC salinity maximum in boreal summer, until appearing as local salinity maxima near 4°S and 4°N in July–August. During late summer and fall, the southern salinity maximum slightly moves southward, probably advected by the poleward transport (Fig. 11d–f). The close qualitative agreement between the bi-monthly climatology from the model and the in situ observations (Figs. 9, 10) confirms that the model is able to reasonably reproduce the salient features of the seasonal cycle in the upper thermocline.

The model outputs allow us also to describe the poorly documented variability of the upper EUC termination and salinity from November to May. During this period, the upper EUC transports high subtropical saline waters along the equator to the eastern GG (Fig. 11f, a–c). At the African coast the EUC flow and its associated saline waters bifurcate meridionally and progressively reform the extra-equatorial maxima between 1.5–3.5°N–S. From January–

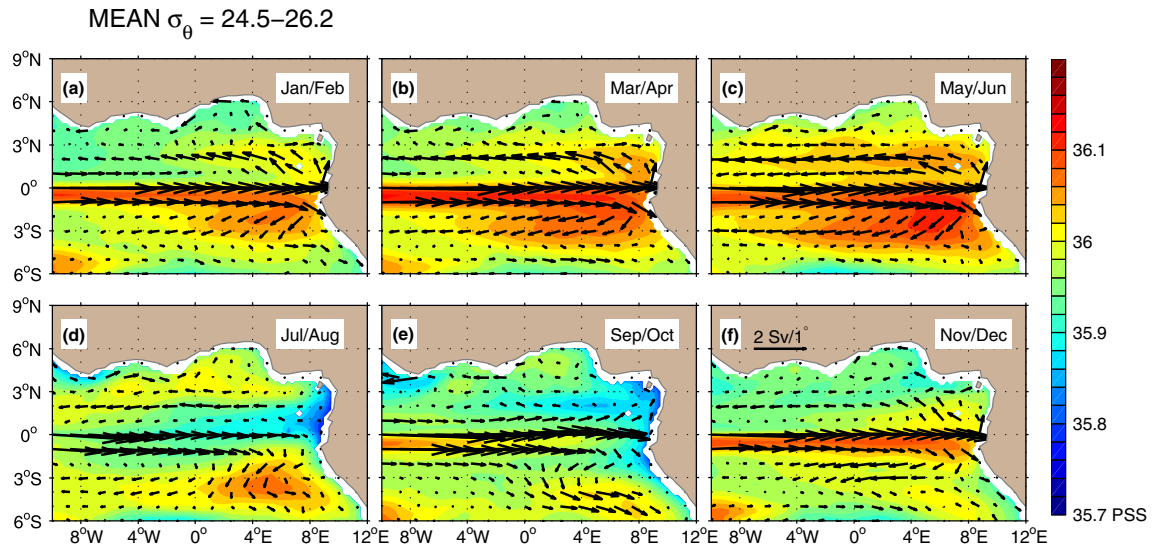

Fig. 11 Bi-monthly climatology of the transport per unit of latitude/longitude (*arrows*; scaling provided in the bottom/right panel) and mean salinity (*shaded color*) in the 24.5–26.2 isopycnal layer in the model. Months from January/February (**a**) to November/December (**f**) are indicated in each subfigure

May, the extra-equatorial westward flow in the upper thermocline transports the saline waters masses westward (Fig. 11a–c).

Note that, in the southern hemisphere a very small poleward transport along the African coast is observed in the upper thermocline, amounting to only 0.2 ± 0.6 Sv across 5°S between 9°E and the coast. Between May and August, the southward export along the African coast is 0.2 Sv while the salinity maximum is eroded in this region. This transport along the African coast is even observed to reverse in September–November ($\sim$0.2 Sv northward), while the salinity is minimum. The poleward transport is maximum during the winter ($\sim$0.4 Sv in December–February), while the salinity re-increases south of the equator along the African coast. Thus, although a direct export of EUC water masses along the African coast found in the model in the coastal GCUC, as previously suggested by Wacongne and Piton (1992), it only represents a very small part of the EUC transport. The EUC recirculates primarily in the westward extra-equatorial branches of the SEC.

In order to better describe the seasonal evolution of the upper thermocline in the GG, we computed the monthly climatology of the depth of the thermocline (materialized here by $\sigma_\theta = 26.2$ isopycnal depth), the vertically-averaged salinity and the zonal transport in the upper thermocline in time-latitude diagrams along 1°E in the center of the GG (Fig. 12). At the equator, the depth of the $\sigma_\theta = 26.2$ and the salinity both exhibit two minima during a climatological year, with the salinity lagging the $\sigma_\theta = 26.2$ depth by about 1 month (Fig. 12a, b). For instance, a first strong minimum in the $\sigma_\theta = 26.2$ depth is observed from June–July to September, while it is observed from July to October for the salinity. The $\sigma_\theta = 26.2$ depth experiences a second weaker minimum in December, leading the second salinity relative minimum observed in January (Fig. 12a, b). On the other hand, the upper EUC transport shows only one minimum in July–August (Fig. 12c).

Off the equator, the $\sigma_\theta = 26.2$ depth is also subject to a semi-annual cycle, with a first strong maximum in March–April and a second maximum of weaker amplitude in October–November (Fig. 12a). In contrast, the extra-equatorial salinity exhibits a dominant annual cycle, with minimum values from September to January (Fig. 12b). At the equator during the late spring, the salinity decreases concomitantly to the $\sigma_\theta = 26.2$ depth and transport, and leads the more progressive poleward erosion of the salinity maxima. Off the equator, from December until the following summer, the salinity maxima are reformed around 2.5°N–S, concomitantly to the deepening of the $\sigma_\theta = 26.2$ depth and the increase of the westward transports (Fig. 12a–c).

The cycle of these three quantities suggests different processes for the boreal summer erosion of the salinity maxima in the GG. At the equator, the strong shallowing of the upper thermocline may contribute to bring its waters near the surface and to increase the vertical shear between the EUC and the surface westward SEC, leading to an enhanced mixing with the surface fresher waters. On the other hand, the dramatic weakening of the EUC transport, starting in late boreal spring, interrupts the supply of saline waters toward the GG. In order to get more insight into the contribution of both advection and mixing in the erosion of saline water, we have computed, in the next section, the

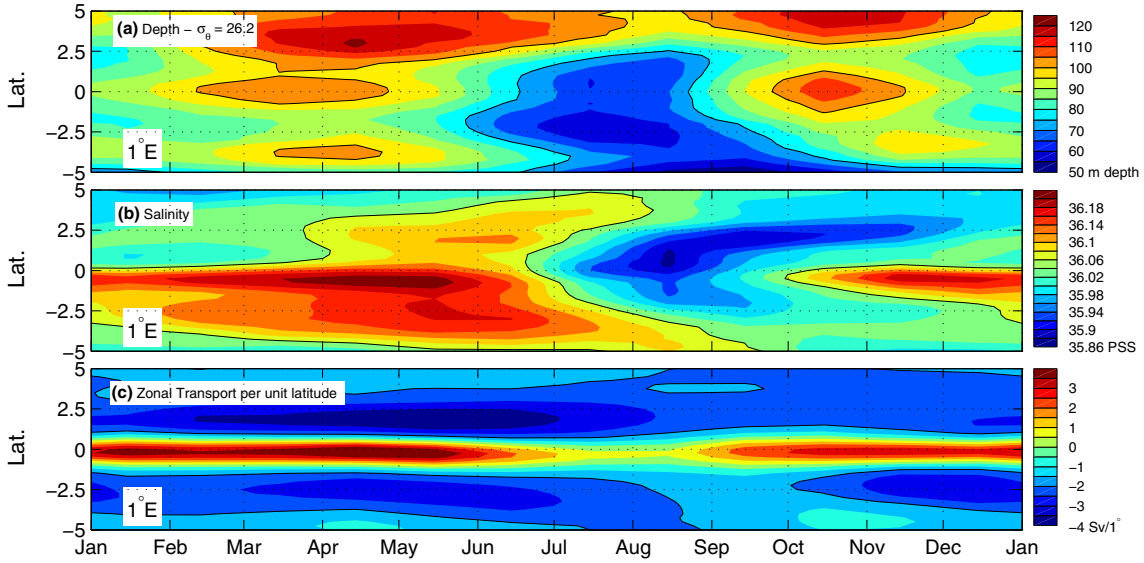

Fig. 12 Time-latitude diagrams of the mean seasonal cycle at 1°E between 5°S–N of **a** $\sigma_\theta = 26.2$ isopycnal depth (in m, *black contour* interval is 20 m), **b** vertically-averaged salinity within the upper thermocline (*black contour* is 36 PSS) and **c** zonal transport per unit latitude in the upper thermocline (in Sv/1°, black contour is 0 Sv/1°)

seasonal salinity budget in the upper thermocline of the eastern GG.

5.2 Seasonal box-averaged salinity budget in the upper thermocline

In order to quantify the role of the ocean circulation (i.e. upper EUC and extra-equatorial recirculation) for the seasonal salinity budget of the upper thermocline, the eastern GG (between 4°W and the African coast) has been decomposed into 3 boxes (Fig. 13): an equatorial box (box 1) between 1.5°S and 1.5°N to represent the upper EUC contribution, a northern box (box 2) between 1.5°N to 5°N and a southern box (box 3) between 1.5°S and 5°S to represent the contributions of the extra-equatorial recirculations on both sides of the equator.

To facilitate the comparison with Fig. 11, we define the mean upper thermocline salinity S_v inside each box as:

$$S_v(t) = \frac{1}{v}\int_{y_S}^{y_N}\int_{x_W}^{x_E}\int_{-h_2}^{-h_1} S(x,y,z,t)\,dxdydz \qquad (1)$$

where v is the total volume of the upper thermocline inside the box.

$$v = \int_{y_S}^{y_N}\int_{x_W}^{x_E}\int_{-h_2}^{-h_1} dxdydz \qquad (2)$$

and S(x,y,z,t) is the local salinity at each grid point, y_S and y_N the latitudes of the southern and northern limits of the box, x_W and x_E the longitudes of the western and eastern limits of the box, and h_1(x,y,z,t) and h_2(x,y,z,t) the depths of the $\sigma_\theta = 24.5$ and $\sigma_\theta = 26.2$ isopycnals which delimit the upper thermocline.

The salinity budget applied to S_v writes:

$$\begin{aligned}\frac{dS_v}{dt} = &-\frac{1}{v}\left[\int_{y_S}^{y_N}\int_{-h_2}^{-h_1} u(S-S_v)dzdy\right]_{x_W}^{x_E}\\ &-\frac{1}{v}\left[\int_{x_W}^{x_E}\int_{-h_2}^{-h_1} v(S-S_v)dzdx\right]_{y_S}^{y_N}\\ &-\frac{1}{v}\left\langle w_1^c(S_1-S_v)\right\rangle+\frac{1}{v}\left\langle w_2^c(S_2-S_v)\right\rangle+Res\end{aligned} \qquad (3)$$

where u and v are the zonal and meridional components of the velocity. The bracket operator denotes the horizontal average over the box: $\langle . \rangle = \int_{x_W}^{x_E}\int_{y_S}^{y_N} .dxdy$. Finally w_1^c and w_2^c are the diapycnal velocities across the $\sigma_\theta = 24.5$ and $\sigma_\theta = 26.2$ surfaces defined as:

$$w_i^c = w_{-h_i} - \frac{\partial h_i}{\partial t} - u\frac{\partial h_i}{\partial x} - v\frac{\partial h_i}{\partial y} \qquad (4)$$

where i = {1, 2} denotes the $\sigma_\theta = 24.5$ and $\sigma_\theta = 26.2$ surfaces and w_{-hi} is the local vertical velocity at depth h_i. The salinity budget (3) is computed offline from the 5-day outputs of the model. In this section, we will only present the monthly climatology of each term of Eq. (3) for the different boxes.

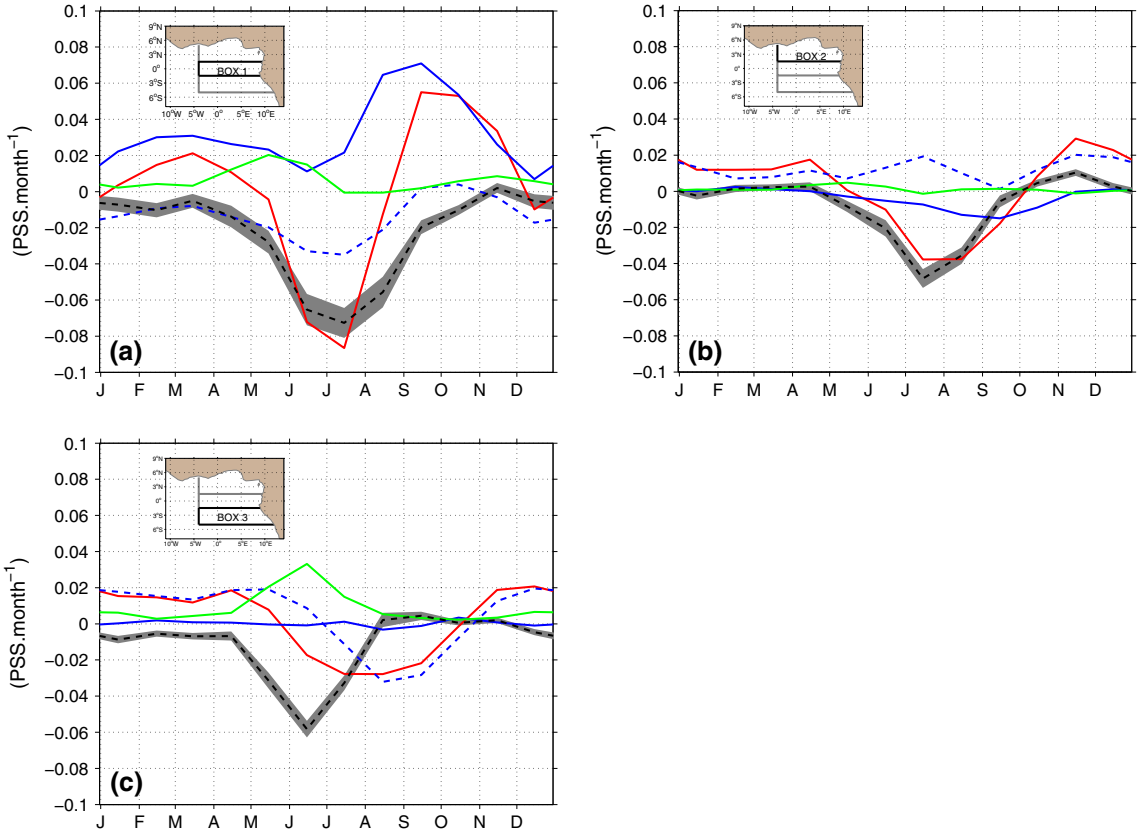

Fig. 13 Seasonal box-averaged salinity budget (in PSS month^{-1}) within the $\sigma_\theta = 24.5$–26.2 layer in the equatorial box 1 (**a**), the northern box 2 (**b**) and the southern box 3 (**c**), as defined in each subfigure mini-map. The box-averaged salinity budget is decomposed in the salinity change rate (*red*), zonal (*solid blue*) and meridional (*dashed blue*) salinity divergence, the salinity divergence due to diapycnal velocities (*green*) and the residual terms with its uncertainty (*black*)

The lhs term of Eq. (3) represents the rate of change of the mean upper thermocline salinity inside the box (in PSS month^{-1}). The first and second rhs terms represent the zonal and meridional divergence of salinity flux in the box. The third and fourth rhs terms represents the cross-isopycnal advective flux of salinity; and *Res* is the residual term induced by the vertical and horizontal diffusivity, and all nonlinear processes that are filtered out in the 5-day outputs of the model. Note, in particular, that the contributions of the intra-seasonal variability, that is known to be important near the equator in the GG (e.g.: Athié and Marin 2008; Han et al. 2008; de Coetlogon et al. 2010; Jouanno et al. 2013), to the meridional eddy fluxes (Peter et al. 2006; de Coetlogon et al. 2010) or to the vertical turbulent mixing above the EUC (Jouanno et al. 2013), cannot be estimated correctly from the 5-day outputs of the model and will thus be included in the residual term.

In Box 1 (Fig. 13a), the salinity change rate reveals two maxima/minima during a climatological year (Fig. 13a, red curve) with a first strongest minimum in June–July (−0.08 PSS month^{-1}) and a second weaker in December (−0.01 PSS month^{-1}). This agrees with the seasonal evolution of the equatorial salinity maximum in the upper thermocline depicted in the previous sections (see Figs. 11, 12). From September to May, the zonal advection of the salinity (Fig. 13a, solid blue curve), mainly due to the zonal divergence in the EUC salinity flux, explains the largest part of this semi-annual cycle. It is partly compensated by the meridional recirculation of EUC salinity in the eastern GG (dashed blue curve). The weakening of the EUC zonal salinity flux and the enhancement of the meridional divergence of the salinity flux contributes to about 25 % of the salinity loss in June–July, during which the residual term (Fig. 13a, solid and dashed black curve) dominates the salinity budget. This suggests that the erosion of the salinity maximum in the EUC core during the cold tongue season is mainly due to enhanced mixing. Note the significant contribution, in April–June, of the diapycnal advective salinity flux mainly through the $\sigma_\theta = 24.5$ surface, that acts to increase salinity and largely compensate the residual term during boreal spring.

The salinity budget in the northern Box 2 is depicted in Fig. 13b. In contrast with the equatorial Box 1, the salinity change rate (Fig. 13b, red curve) presents a predominant

annual cycle characterized by a salinity increase from October to April (maximum 0.02 PSS month^{-1}), and a salinity decrease from May to October (minimum −0.04 PSS month^{-1}). During the winter–spring season, the salinity increase is mainly explained by the meridional advection of salinity into the box (Fig. 13b, dashed blue curve), while during the boreal late spring and summer, the loss is mainly explained by the residual term (Fig. 13b, dashed black curve), i.e. mixing. The diapycnal flux of salt remains negligible throughout the year (Fig. 13b, green curve).

In the southern Box 3 (Fig. 13c) as for the northern box 2, the salinity change rate (Fig. 13c, red curve) shows a dominant annual cycle with a freshening from May to October (minimum −0.03 PSS month^{-1}), and an increase of salinity from September to April (maximum 0.02 PSS month^{-1}), *i.e.* in phase with the northern and equatorial boxes. The meridional advection of salinity (dashed blue curve) from the EUC recirculation explains the salinity increase from October to April as for the two other boxes. In contrast, from August to October, the meridional advection of salinity across 5°S is the main contributor to the freshening. This freshening can be explained by the southward displacement, in late summer and fall, of the southern salinity maximum, that is observed in the south–eastern part of the GG around 4–6°S in Fig. 11d, e. The residual term only contributes from April to August, participating to the erosion of the salinity maximum in boreal summer, and is partly compensated by the cross-isopycnal advective flux.

In summary, the strong diminution of salinity noticed during the late spring and summer in the equatorial box 1 is firstly explained by the residual term. This term represents the vertical and horizontal mixing that contributes to the bulk of erosion in the upper equatorial thermocline (about 75 %), plus the possible effect of meridional eddy flux due to intraseasonal variability. The dramatic weakening of the salinity advection by the EUC at 4°W contributes also to about 25 % of the diminution of equatorial salinity. In the extra-equatorial boxes, the mixing term appears also to play a dominant role in eroding the salinity maxima during the late spring and summer, while meridional advection acts to supply extra-equatorial maxima of salinity with saline waters from the EUC in winter and spring. It is also interesting to note the north–south asymmetry during the erosion of extra-equatorial salinity maxima: north of the equator, the salinity erosion is mainly due to mixing, while south of the equator the salinity maximum is first partially eroded by mixing (between May–July) then advected southward.

5.3 Role of equatorial zonal wind

In this section, we diagnose the potential mechanisms that could explain the dominant role of the mixing in the seasonal variability of the EUC termination and associated salinity maximum erosion in the eastern GG from the model. As shown by several previous studies (e.g., Katz 1984; Verstraete 1992; Arhan et al. 2006; Hormann and Brandt 2007; Ding et al. 2009; Kolodziejczyk et al. 2009; Jouanno et al. 2011b), the equatorial zonal wind forcing plays a leading role by driving the surface current and the seasonal baroclinic adjustment of the upper eastern equatorial Atlantic, *i.e.* by strengthening the vertical shear between the surface and subsurface currents.

Figure 14 presents the seasonal variability of the zonal wind stress (averaged between 1.5°S–N) along the equator. East of 30°W, it shows a seasonal cycle with two maxima/minima, which acts to seasonally increase (from May to August and from October to January) and decrease (from January to April and from August to October) the permanent Easterlies west of 10°W. In the GG, between 5°W and 5°E, this semi-annual cycle leads to a seasonal reversal of the zonal wind stress between 5°W and 5°E, with strongest Easterlies in May–June and strongest Westerlies in September, and secondary extrema of zonal wind stress anomalies in November (weak Easterlies) and January–February (weak Westerlies). Note the phase lag between the semi-annual cycles west of 10°W and east of 10°W.

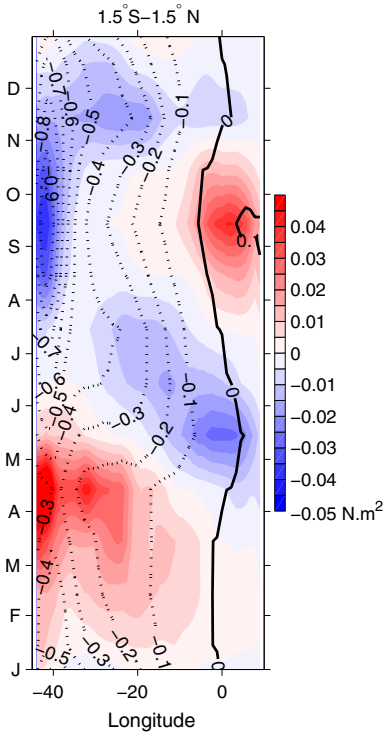

Fig. 14 Longitude-time diagram of the mean seasonal anomaly of the zonal wind stress (colors) and total mean zonal wind stress (contours) averaged between 1.5°S–N and between 45°W and 10°E computed from 1993–2007 DFS wind forcing dataset. Unit is N m^{-2}

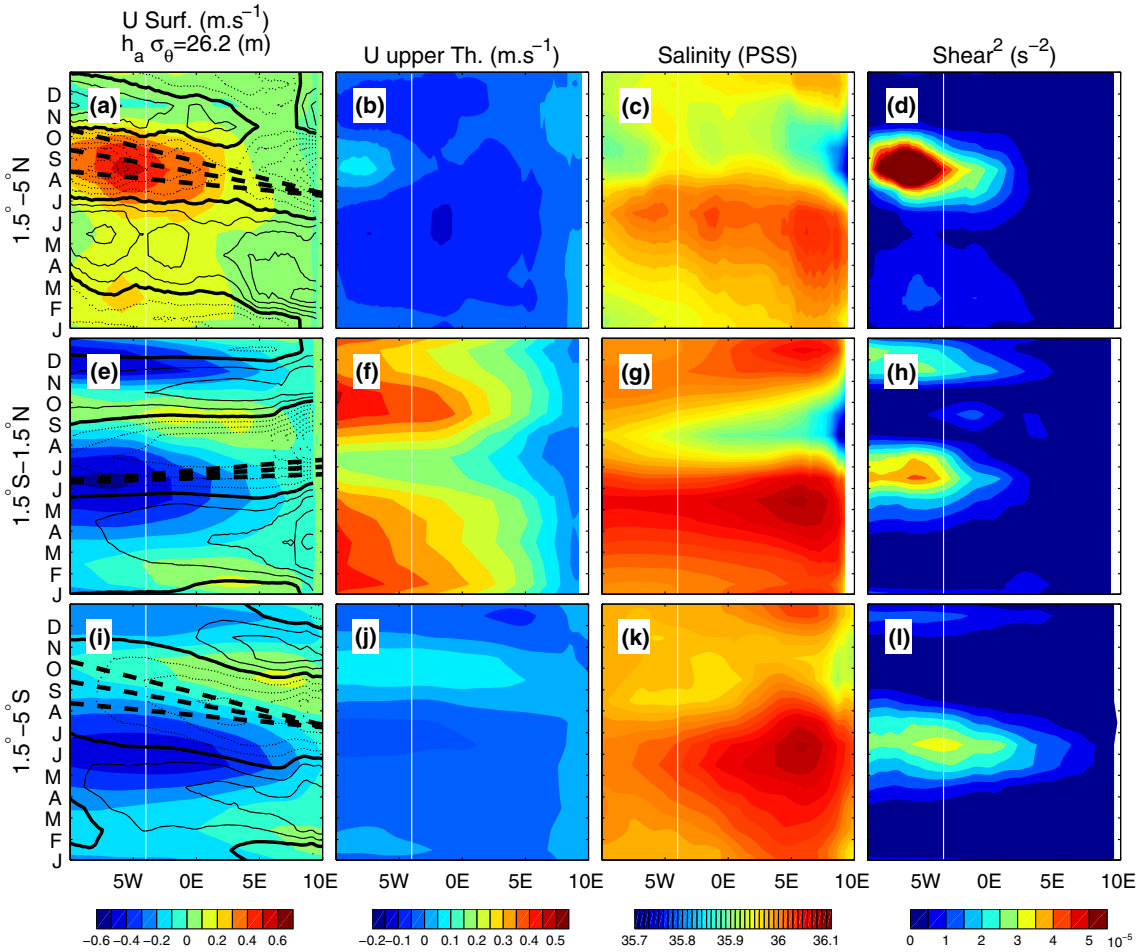

Fig. 15 Longitude-time diagrams of mean seasonal cycle of (**a**) the surface zonal velocities (in m s^{-1}) and the seasonal anomaly of the $\sigma_\theta = 26.2$ depth (in m; CI = 5 m; positive anomalies are in *solid line*); **b** the EUC mean velocities in the upper thermocline (in m s^{-1}); **c** mean salinity in the upper thermocline (in PSS); and **d** the mean vertical shear (in s^{-2}) between the upper thermocline and the surface averaged between 1.5°N–5°N. The white line at 4°W materializes the western boundary of the boxes in Fig. 10. (**e**–**h**) same as (**a**–**d**), but between 1.5°S–N. (**i**–**l**): same as (**a**–**d**), but between 5°s^{-1}.5°S. The *dashed black lines* represent the characteristics of the propagation speed respectively for a Kelvin wave of the first (2.14 m s^{-1}), second (1.24 m s^{-1}) and third (0.86 m s^{-1}) baroclinic modes (**e**); and for long Rossby waves of the first (0.71 m s^{-1}), second (0.41 m s^{-1}) and third (0.29 m s^{-1}) baroclinic modes (in **a** and **i**)

We now discuss the seasonal cycle of the EUC and its associated saline waters in the light of the seasonal variability of the equatorial zonal wind and the surface currents. Figure 15 depicts the mean seasonal cycle for the surface zonal currents and upper thermocline depth—materialized by the $\sigma_\theta = 26.2$ isopycnal depth (first column; Fig. 15a, e, i), the vertically-averaged zonal velocities (second column; Fig. 15b, f, j) and salinity (third column; Fig. 15c, g, k) in the upper thermocline, and the vertical shear of zonal velocities computed from the surface current and the upper thermocline vertically-averaged velocities (last column; Fig. 15d, h, l).

At the equator, the semi-annual cycle of the zonal wind stress forces a semi-annual cycle of the zonal current at the surface, that manifests by a westward intensification in boreal spring–summer and during November, and an eastward reversal during early fall and winter (Fig. 15e; color shading). The seasonal variability of the upper thermocline depth anomalies also presents a semi-annual cycle in quadrature (3-month phase lag) with the semi-annual cycle of the surface current (Fig. 15e). This lag is characteristic of the linear basin mode adjustment to the semi-annual cycle of the equatorial wind stress described in Cane and Moore (1981) or Ding et al. (2009). During the late spring–summer and November–December periods, the intensification of the surface currents and the shallowing of the upper thermocline are concomitant with the erosion of the EUC velocity and its associated salinity maximum (Fig. 15f, g). Hence, as the surface current increases and the thermocline heaves up, the vertical shear between the EUC and the surface current is strongly enhanced at the equator (Fig. 15h).

North and south of the equator, the upper thermocline depth anomalies (Fig. 15a, i) show a seasonal cycle associated with a more marked annual component than at the equator (Fig. 15e). In the southern hemisphere, the surface zonal velocities exhibit a semi-annual cycle comparable with those along the equator (Fig. 15e, i), while in the northern part of the GG, the currents are mostly eastward with a more marked annual cycle (Fig. 15a). The upper thermocline depth anomalies exhibit a westward propagation visible in Fig. 15a and i, that is slower in the southern hemisphere (between second and third baroclinic mode) than in the northern hemisphere (less than the first baroclinic mode). In the upper thermocline layer, the currents are westward on both sides of the EUC and exhibit a weak variability (Fig. 15b, j), while the salinity experiences a dominant annual cycle with a weakening from late spring to winter (Fig. 15c, k). In the southern hemisphere, the vertical shear of the zonal velocities is enhanced following a semi-annual cycle that is in phase, though of lesser amplitude, with the one at the equator (Fig. 15l, h). In contrast, in the northern hemisphere, the vertical shear is intensified during the westward intensification of the surface currents during the late winter and summer (Fig. 15d).

At the equator, these diagnostics suggest that the salinity maximum in the eastern GG is supplied by the EUC, and that the salinity content and the EUC are subject to the same seasonality. In the surface layer above the EUC, the semi-annual cycle of the SEC is associated with the basin adjustment of a second baroclinic basin mode to the semi-annual cycle of the equatorial zonal wind (Ding et al. 2009). This adjustment manifests by the acceleration of the SEC between 5°N–S due to the propagation of westward Rossby waves from the eastern boundary of the GG, that transport the saline water masses westward on the both flanks of the EUC during the boreal late spring. The adjustment is compatible with the propagation velocities observed at the equator and in the southern hemisphere, but not in the northern hemisphere. This discrepancy is probably due to the effects of the northern coast in the GG that dramatically modifies the meridional structure of the equatorial waves (Cane and Sarachik 1983). During the late boreal spring and summer, the intensification of the westward equatorial wind accelerates the SEC at the surface and heaves the thermocline up at depth. The upper thermocline is pinched off and the EUC saline water masses are simultaneously eroded. It results that no more saline waters can be advected in the eastern GG and recirculate in the extra-equatorial branches. The decrease of EUC transport, along with the erosion of its associated salinity maximum, can thus be explained by the vertical mixing induced by the stronger vertical shear between the surface and upper thermocline currents during boreal spring and fall, in agreement with results by Jouanno et al. (2011b).

6 Discussion and conclusion

This paper describes in a first part the time evolution of EUC water masses during boreal summer in the eastern equatorial Atlantic from a new set of in situ observations including both currents and salinity measurements. It provides strong observational evidence of the existence of an intense seasonal variability of the circulation and salinity in the upper thermocline in the GG from boreal late spring to fall. The more striking signature of this variability is the presence of westward extra-equatorial recirculations of EUC water masses in late boreal spring (early summer) and the absence of a direct supply of EUC saline water masses from the west in mid and late summer. This is due to (i) the progressive weakening of the upper thermocline EUC in the GG in boreal summer, and (ii) the concomitant erosion of the salinity maximum west of the GG induced by the outcropping of the thermocline in the mixed layer (Voituriez 1983; Verstraete 1992) and/or by enhanced vertical diffusion in the surface layer (Gouriou and Reverdin 1992; Jouanno et al. 2011a). All seven cruises and Argo observations used in this study support this seasonal cycle. Some observed differences between repeated sections however suggest some inter-annual and/or intra-seasonal variability (Marin et al. 2009).

In situ cruises observations used in this study were mostly collected between June and November, thus preventing us from analyzing the complete seasonal cycle of the upper thermocline circulation. Therefore, in order to study the complete seasonal variability of the termination of the EUC and the fate of associated saline waters in the GG, we used validated NEMO model outputs from 1993 to 2007 and compared them with the repeated cruises sections, as previously done at 10°W by Kolodziejczyk et al. (2009).

Simulations of the upper layers of the eastern equatorial Atlantic Ocean are known to be strongly sensitive to the parameterization of the vertical mixing (Pacanowski and Philander 1981; Wacongne 1989; Blanke and Delecluse 1993). Considering the high sensitivity of the EUC properties to the vertical viscosity in the models (Böning and Kröger 2005), vertical mixing is suspected to be responsible for the bias in salinity observed in the upper thermocline in the model, and the discrepancy of the stratification and EUC strength reported in the model validation section. However, in boreal summer the model is qualitatively consistent with the variability observed in our data set but also in several previous observations in the region (Hisard and Morlière 1973; Verstraete 1992; Gouriou and Reverdin 1992; Mercier et al. 2003; Bourlès et al. 2002), thus confirming the seasonal cycle suggested by the sparse observations.

The analysis of the mean seasonal variability of the upper thermocline has established a robust seasonal cycle.

The model allowed us to quantify the seasonal salinity budget in the upper thermocline in the eastern GG. It appears first that the amount of saline waters in the upper thermocline of the GG is strongly dependent of the upper EUC transport that contributes to feed the eastern GG and extra-equatorial salinity maxima, mainly during the boreal spring. Such a feature is consistent with the earlier observations made in 1995 by Mercier et al. (2003). A direct poleward recirculation of the EUC water masses along the African Coast in the coastal GCUC was suggested by Wacongne and Piton (1992). Our observations do not allow to sample the GCUC which remains poorly documented in the literature (Wacongne and Piton 1992). The existence of such an along-coast EUC continuation is also suggested in the model. However, it only exports about 0.2 ± 0.6 Sv of upper thermocline water masses southward, which represents only a very small part of the EUC transport.

From May to September, the upper EUC transport in the west of the GG is minimum in the model and advects no more saline water masses into the GG, as suggested by previous observations (Gouriou and Reverdin 1992; Kolodziejczyk et al. 2009). West of 10°W, Jouanno et al. (2011a, b, 2013) demonstrated that the enhancement of vertical mixing during this season strongly contributes to the cooling of the subsurface temperature at the upper bound of the EUC. In the GG, Da-Allada et al. (2014) have recently shown from a numerical study an increase of the mixed layer salinity during boreal late spring and summer. This increase results from the dominance of the vertical diffusion of subsurface saline waters over they freshwater surface advection originating from river run off in the eastern GG during this period. Our study suggests that the intensified vertical mixing also contributes to erode the upper EUC and its salinity maximum not only west of 10°W, thus explaining the reduction of the saline waters advected in the eastern GG, but also in the GG between 4°S and 4°N to locally entrain waters from the upper EUC into the surface mixed layer. The vertical mixing may contribute to the progressive erosion of the equatorial and extra-equatorial maxima of salinity during boreal summer, in agreement with the enhancement of our residual term of salinity (loss) during this season. However, in the GG, the local vertical mixing may be not the unique mechanism responsible for the seasonal erosion of salinity, and our results indeed indicate that the contribution of horizontal advection to the seasonal cycle is also important, in particular during the second part of the year (Fig. 12). Though the vertical mixing is not as strong in the eastern as in the western GG, it remains a dominant contributor to the mixed layer heat budget (Jouanno et al. 2011a, b; Da-Allada et al. 2014, Berger et al. 2014) and to the upper salinity budget (Da-Allada et al. 2013). In the GG, the contribution of vertical mixing to the salinity budget in the eastern GG can also be distant, through the advection of less saline waters that have been previously freshened through turbulent vertical mixing by surface waters in the west (between 20°W and 0°E). In the easternmost part of the GG, the strong surface desalinization due to the rivers' runoff is likely to also play a significant role in the dynamical and salinity balance of the upper GG (Hisard 1973; Jouanno et al. 2011a; Da-Allada et al. 2013). Following model results from Berger et al. (2014), the lateral mixing and eddy diffusivity could also play a significant role in eroding the EUC and extra-equatorial salinity maximum. Finally, some intra-seasonal features like the 15-day variability observed near the equator in the GG (Athié and Marin 2008; de Coetlogon et al. 2010; Jouanno et al. 2013), could contribute to the erosion of salt during boreal summer.

From boreal fall to winter, the EUC appears to reinforce in the upper thermocline, bringing back saline water masses into the eastern GG, which progressively spreads along the coast in the equatorial band and supplies again the extra-equatorial salinity maxima. During December–January, the salinity and upper thermocline are slightly eroded. This is reminiscent to the reinforcement of the surface current and of the second weaker upwelling that is present from November to January in the central and eastern equatorial Atlantic, as suggested by Arhan et al. (2006), Okumura and Xie (2006), Ding et al. (2009) or Jouanno et al. (2011a).

Ding et al. (2009) have studied the seasonal cycle of the sea surface height (SSH) and surface currents in equatorial Atlantic. They have shown that the thermocline and surface currents adjust to the semi-annual cycle of the zonal wind over the Atlantic basin. The reinforcement of the wind during boreal spring and fall induces the semi-annual intensification of the surface currents and of the thermocline upwelling in the GG that is in return enhanced by a semi-annual basin mode. Some other studies (e.g., Houghton 1983; Hormann and Brandt 2007; Ding et al. 2009) have linked the seasonal variability in the upper ocean in the GG to a basin scale adjustment to the seasonal variations in easterlies. This equatorial adjustment manifests in late boreal spring by the propagation of an upwelling Kelvin wave that reflects into equatorial Rossby waves at the African coast (Philander 1986; Ding et al. 2009). The semi-annual reinforcement of the surface currents plays a key role in the enhancement of turbulent mixing that erodes the upper EUC in the central Atlantic (Jouanno et al. 2011a).

An important aspect of the variability of the termination of the EUC in the GG is the fate of its saline water masses of subtropical origin involved in the larger meridional circulation of STC and TC (e.g., Blanke et al. 2002; Snowden and Molinari 2003; Zhang et al. 2003; Hazeleger and De Vries 2003; Molinari et al. 2003; Wang 2005). The

seasonal variability of the EUC termination and associated salinity maximum inferred from both the observations and the model reveals slightly different features than the STC mean circulation picture. During the first part of the year, the EUC water masses rather appears to join the eastern boundary of the equatorial Atlantic and to recirculate off the equator within the upper thermocline, without any contact with the surface. During boreal spring and summer, and November–December, the erosion of the upper EUC termination and saline waters is strongly associated with the upwelling intensity through vertical advection and mixing. The exact contribution of this seasonal cycle for the mean view of the STC would require further analysis.

Acknowledgments Based on a French initiative, AMMA was built by an international scientific group and was funded by a large number of agencies, from France, UK, US and Africa. It benefited of a major financial contribution from the European Community's Sixth Framework Research Programme. Refer to: http://www.amma-international.org for detailed information on this program. The authors also thank the PIRATA program for providing for free precious data sets to the whole scientific community. Authors do thank Jacques Grelet, Fabrice Roubaud, Rémy Chuchla and vessels' crews who make possible the in situ data acquisition during all EGEE/AMMA and yearly PIRATA cruises. The Argo data are validated and kindly provided by Fabienne Gaillard (LPO, CNRS/Ifremer/IRD/UBO, Brest, France), and funded by the CNES-TOSCA project 'GLOSCAL'. Authors do also thank Anne-Marie Tréguier for valuable discussions on NEMO simulations, and anonymous reviewers for constructive remarks that helped to substantially improve the manuscript.

References

Antonov JI, Seidov D, Boyer TP, Locarnini RA, Mishonov AV, Garcia HE, Baranova OK, Zweng MM, Johnson DR (2010) World ocean atlas 2009, volume 2: salinity. In: Levitus S (ed) NOAA atlas NESDIS 69, U.S. Government Printing Office, Washington, DC, 184 pp

Arhan M, Tréguier AM, Bourlès B, Michel S (2006) Diagnosing the annual cycle of the equatorial undercurrent in the Atlantic Ocean from a general circulation model. J Phys Oceanogr 36:1502–1522

Athié G, Marin F (2008) Cross-equatorial structure and temporal modulation of intraseasonal variability at the surface of the Tropical Atlantic Ocean. J Geophys Res 113:C08020. doi:10.1029/2007JC004332

Barnier B, Marchesiello P, de Miranda AP, Molines JM, Coulibaly M (1998) A sigma-coordinate primitive equation model for studying the circulation in the South Atlantic. Part I: model configuration with error estimates. Deep Sea Res 45:543–572

Barnier B, Madec G, Penduff T, Molines J-M, Tréguier A-M, Le Sommer J, Beckmann A, Biastoch A, Böning C, Dengg J, Derval C, Durand E, Gulev S, Remy E, Talandier C, Theetten S, Maltrud M, McClean J, De Cuevas B (2006) Impact of partial steps and momentum advection schemes in a global ocean circulation model at eddy permitting resolution. Ocean Dyn 4. doi:10.1007/s10236-006-0082-1

Berger H, Treguier A-M, Perenne N, Talandier C (2014) Dynamical contribution to sea surface salinity variations in the eastern Gulf of Guinea base on numerical modelling. Clim Dyn (submitted)

Blanke B, Delecluse P (1993) Variability of the tropical Atlantic Ocean simulated by a general circulation model with two different mixed-layer physics. J Phys Oceanogr 23:1363–1388

Blanke B, Arhan M, Lazar A, Prévost G (2002) A Lagrangian numerical investigation of the origins and fates of the salinity maximum water in the Atlantic. J Geophys Res 107(C10):3163. doi:10.1029/2002JC001318

Böning CW, Kröger J (2005) Seasonal variability of deep currents in the equatorial Atlantic: a model study. Deep Sea Res I 52:99–121

Bourlès B, Gouriou Y, Chuchla R (1999) On the circulation in the upper layer of the western equatorial Atlantic. J Geophys Res 104:21151–21170

Bourlès B, D'Orgeville M, Eldin G, Gouriou Y, Chuchla R, du Penhoat Y, Arnault S (2002), On the evolution of the thermocline and subthermocline eastward currents in the equatorial Atlantic. Geophys Res Lett 29. doi:10.1029/2002GL015098

Bourlès B, Brandt P, Caniaux G, Dengler M, Gouriou Y, Key E, Lumpkin R, Marin F, Molinari RL, Schmid C (2007) African monsoon multidisciplinary analysis (AMMA): special measurements in the tropical Atlantic. CLIVAR Exch Lett 41(12):2

Bourlès B, Lumpkin R, McPhaden MJ, Hernandez F, Nobre P, Campos E, Yu L, Planton S, Busalacchi A, Moura AD, Servain J, Trotte J (2008) The PIRATA program: history, accomplishments and future directions. Bull Am Meteorol Soc 89:1111–1125

Brandt P, Schott FA, Provost C, Kartavtseff A, Hormann V, Bourlès B, Fischer J (2006) Circulation in the central equatorial Atlantic: mean and intraseasonal to seasonal variability. Geophys Res Lett 33:L07609. doi:10.1029/2005GL025498

Brodeau L, Barnier B, Tréguier A-M, Penduff T, Gulev S (2010) An ERA-40-based atmospheric forcing for global ocean circulation models. Ocean Model 31:88–104

Cane MA, Moore DW (1981) A note on low-frequency equatorial basin modes. J Phys Oceanogr 11:1578–1584

Cane MA, Sarachik ES (1983) Equatorial oceanography. Rev Geophys 21:1137–1148

Chang P, Zhang R, Hazeleger W, Wen C, Wan X, Ji L, Haarsma RJ, Breugem W-P, Seidel H (2008) Oceanic link between abrupt changes in the north Atlantic Ocean and the African monsoon. Nature 1:444–448

Da-Allada CY, Alory G, du Penhoat Y, Kestenare E, Durand F, Hounkonnou NM (2013) Seasonal mixed-layer salinity balance in the tropical Atlantic Ocean: mean state and seasonal cycle. J Geophys Res 118:332–345. doi:10.1029/2012JC008357

Da-Allada CY, du Penhoat Y, Jouanno J, Allory G, Hounkonnou NM (2014) Mixed layer salinity balance in the Gulf of Guinea: seasonal and interannual variability. Clim Dyn (submitted)

Dai A, Trenberth KE (2002) Estimates of freshwater discharge from continents: latitudinal and seasonal variations. J Hydrometeorol 3:660–687

de Coetlogon G, Janicot S, Lazar A (2010) Intra-seasonal variability of the ocean-atmosphere coupling in the Gulf of Guinea during boreal spring and summer. Q J Roy Meteorol Soc 136:426–441

Ding H, Keenlyside NS, Latif M (2009) Seasonal cycle in the upper equatorial Atlantic Ocean. J Geophys Res 114:C09016. doi:10.1029/2009JC005418

Gaillard F, Autret E, Thierry V, Galaup P, Coatanoan C, Loubrieu T (2009) Quality control of large Argo data sets. J Atmos Ocean Technol 26(2):337–351

Giarolla E, Nobre P, Malagutti M, Pezzi LP (2005) The Atlantic equatorial undercurrent: PIRATA observations and simulations with GFDL modular ocean model at CPTEC. Geophys Res Let 32. doi:10.1029/2004GL022206

Gouriou Y, Reverdin G (1992) Isopycnal and diapycnal circulation of the upper equatorial Atlantic Ocean in 1983–1984. J Geophys Res 97:3543–3572

Grodsky SA, Carton JA (2002) Surface drifter pathways originating in the equatorial Atlantic cold tongue. Geophys Res Lett 29:2147. doi:10.1029/2002GL015788

Han W, Webster PJ, Lin J-L, Liu WT, Fu R, Yuan D, Hu A (2008) Dynamics of intraseasonal sea level and thermocline variability in the equatorial Atlantic during 2002–03. J Phys Oceanogr 38:945–966

Hazeleger W, de Vries P (2003) Fate of the equatorial undercurrent in the Atlantic. In Goni GJ, Malanotte-Rizzoli P (eds) Interhemispheric water exchange in the Atlantic ocean. Amsterdam, Elsevier, pp 175–191

Hazeleger W, de Vries P, Friocourt Y (2003) Sources of the equatorial undercurrent in the Atlantic in a high-resolution ocean model. J Phys Oceanogr 33:677–693

Hisard P (1973) Variations saisonnières à l'équateur dans le Golfe de Guinée, *Cah.* ORSTOM Sér Océanogr XI: 349–358

Hisard P, Morlière A (1973), La terminaison du contre-courant équatorial subsuperficiel atlantique (courant de Lomonosov) dans le Golfe de Guinée, *Cah.* ORSTOM, Sér Océanogr XI:455–464

Hormann V, Brandt P (2007) Atlantic Equatorial Undercurrent and associated cold tongue variability. J Geophys Res 112:C06017. doi:10.1029/2006JC003931

Houghton RW (1983) Seasonal variations of the subsurface thermal structure in the Gulf of Guinea. J Phys Oceanogr 13:2070–2081

Hummels R, Dengler M, Bourlès B (2013) Seasonal and regional variability of upper ocean diapycnal heat flux in the Atlantic Cold Tongue. Prog Oceanogr 111:52–74

Johns WE, Brandt P, Bourlès B, Tantet A, Papapostolou A, Houk A (2014) Zonal structure and seasonal variability of the atlantic equatorial undercurrent. Clim Dyn (submitted)

Jouanno J, Marin F, du Penhoat Y, Sheinbaum J, Molines JM (2011a) Seasonal heat balance in the upper 100 m of the Equatorial Atlantic Ocean. J Geophys Res 116:C09003. doi:10.1029/2010JC006912

Jouanno J, Marin F, du Penhoat Y, Molines JM, Sheinbaum J (2011b) Seasonal modes of surface cooling in the Gulf of Guinea. J Phys Oceanogr 41:1408–1416. doi:10.1175/JPO-D-11-031.1

Jouanno J, Marin F, du Penhoat Y, Molines JM (2013) Intraseasonal modulation of the surface cooling in the Gulf of Guinea. J Phys Oceanogr 43:382–401. doi:10.1175/JPO-D-12-053.1

Katz E (1984) Basin wide thermocline displacements along the equator of the Atlantic in 1983. Geophys Res Lett 11:729–732. doi:10.1029/GL011i008p00729

Katz E, Molinari RL, Cartwright D, Hisard P, Lass H, deMesquita A (1981) The seasonal transport of the Equatorial Undercurrent in the western Atlantic (during the Global Weather Experiment). Ocean Acta 4:445–450

Kolodziejczyk N, Bourlès B, Marin F, Grelet J, Chuchla R (2009) Seasonal variability of the equatorial undercurrent at 10 W as inferred from recent in situ observations. J Geophys Res 114:C06014. doi:10.1029/2008JC004976

Locarnini RA, Mishonov AV, Antonov JI, Boyer TP, Garcia HE, Baranova OK, Zweng MM, Johnson DR (2010) World Ocean Atlas 2009, Volume 1: Temperature. In: S. Levitus (ed) NOAA Atlas NESDIS 68, U.S. Government Printing Office, Washington, DC, 184 pp

Lumpkin R, Speer K (2003) Large-scale vertical and horizontal circulation in the North Atlantic Ocean. J Phys Oceanogr 33:1902–1920. doi:10.1175/1520-0485(2003)033<1902:LVAHCI>2.0.CO;2

Madec G (2008) NEMO ocean engine: version3.1, Note du Pôle de modélisation de l'IPSL n°27

Marin F, Caniaux G, Giordani H, Bourlès B, Gouriou Y, Key E (2009) Why were sea surface temperatures so different in the eastern equatorial Atlantic in June 2005 and 2006? J Phys Oceanogr 39:1416–1431

Mercier H, Arhan M, Lutjeharms J (2003) Upper-layer circulation in the eastern equatorial and South Atlantic Ocean in January–March 1995. Deep Sea Res I 50:863–887

Molinari RL, Bauer S, Johnson GC, Bourlès B, Gouriou Y, Mercier H (2003) A comparison of kinematic evidence for tropical cells in the Atlantic and Pacific oceans. In: Goni GJ, Malanotte-Rizzoli P (eds) Interhemispheric water exchange in the Atlantic Ocean. Elsevier, Amsterdam

Okumura Y, Xie S-P (2006) Some overlooked features of Tropical Atlantic climate leading to a new Niño-like Phenomenon. J Clim 19:5859–5874

Pacanowski RC, Philander SGH (1981) Parameterization of vertical mixing in numerical models of Tropicals Oceans. J Phys Oceanogr 11:1443–1451

Peter A-C, Le Hénaff M, du Penhoat Y, Menkes CE, Marin F, Vialard J, Caniaux G, Lazar A (2006) A model study of the seasonal mixed layer heat budget in the equatorial Atlantic. J Geophys Res 111:C06014. doi:10.1029/2005JC003157

Philander SGH, Pacanowski R (1986) A model of the seasonal cycle of the Tropical Atlantic ocean. J Geophys Res 91:14192–14206

Redelsperger J-L, Thorncroft CD, Diedhiou A, Lebel T, Parker DJ, Polcher J (2006) African monsoon multidisciplinary analysis: an international research project and field campaign. Bull Am Meteorol Soc 87:1739–1746

Rhein M, Dengler M, Sültenfuß J, Hummels R, Hüttl-Kabus S, Bourlès B (2010) Upwelling and associated heat flux in the equatorial Atlantic inferred from helium isotope disequilibrium. J Geophys Res 115:C08021. doi:10.1029/2009JC005772

Richardson P, Reverdin G (1987) Seasonal cycle of velocity in the Atlantic NECC as measured by surface drifters, current meters and ship drifts. J Geophys Res 92:3691–3708

Schott FA, Fischer J, Stramma L (1998) Transports and pathways of the upper-layer circulation in the western tropical Atlantic. J Phys Oceanogr 28:1904–1928

Snowden D, Molinari RL (2003), Subtropical cells in the Atlantic ocean: an observational summary. In: Goni GJ, Malanotte-Rizzoli P (eds) Interhemispheric water exchange in the Atlantic Ocean. Elsevier Oceanography Series 68:287–312

Stramma L, Schott F (1999) The mean flow field of the tropical Atlantic Ocean. Deep Sea Res II 46(1–2):279–303

Tréguier A-M, Barnier B, De Miranda AP, Molines JM, Grima N, Imbard N, Madec G, Messager C (2001) Eddy permitting model of the Atlantic circulation: evaluating open boundary conditions. J Geophys Res 106(C10):22115–22129. doi:10.1029/2000JC000376

Verstraete J-M (1992) The seasonal upwellings in the Gulf of Guinea. Prog Oceanogr 29:1–60

Voituriez B (1983) Les variations saisonnières des courants équatoriaux à 4°W et l'upwelling équatorial du Golfe de Guinée, I. Le sous-courant équatorial. Oceanogr Trop 18(2): 163–183

Wacongne S (1989) Dynamical regimes of fully nonlinear stratified model of the Atlantic Equatorial Undercurrent. J Geophys Res 94(C4):4801–4815

Wacongne S, Piton B (1992) The near-surface circulation in the northeastern corner of the South Atlantic Ocean. Deep-Sea Res 39:1273–1298

Wade M, Caniaux G, du Penhoat Y (2011) Variability of the mixed layer heat budget in the eastern equatorial Atlantic during 2005–2007 as inferred using Argo floats. J Geophys Res 116:C08006. doi:10.1029/2010JC006683

Wang C (2005) Subthermocline tropical cells and equatorial subsurface countercurrents. Deep-Sea Res I 52:123–135

Zhang D, McPhaden MJ, Johns WE (2003) Observational evidence for flow between the subtropical and tropical Atlantic: the Atlantic subtropical cells. J Phys Oceanogr 33:1783–1797